| | |
|---|---|
| ***Publication Year*** | 2016 |
| ***Acceptance in OA*** | 2020-05-04T09:14:04Z |
| ***Title*** | Simulation and modeling of silicon pore optics for the ATHENA x-ray telescope |
| ***Authors*** | SPIGA, Daniele, Christensen, Finn Erland, Bavdaz, Marcos, CIVITANI, Marta Maria, Conconi, Paolo, Della Monica Ferreira, D., Knudsen, Erik, Massahi, Sonny, PARESCHI, Giovanni, SALMASO, Bianca, Shortt, Brian, Tayabaly, Kashmira, Westergaard, Niels, Wille, Erik |
| ***Publisher's version (DOI)*** | 10.1117/12.2232230 |
| ***Handle*** | http://hdl.handle.net/20.500.12386/24411 |
| ***Serie*** | PROCEEDINGS OF SPIE |
| ***Volume*** | 9905 |

# Simulation and modeling of silicon pore optics for the ATHENA X-ray telescope

D. Spiga[1], F.E. Christensen[2], M. Bavdaz[3], M.M. Civitani[1], P. Conconi[1], D. Della Monica Ferreira[2], E.B. Knudsen[4], S. Massahi[2], G. Pareschi[1], B. Salmaso[1], B. Shortt[3], K. Tayabaly[1,5], N.J. Westergaard[2], E. Wille[3]

[1]INAF – Brera Astronomical Observatory, Via Bianchi 46, 23807, Merate (Italy)
[2]DTU Space, Techn. Univ. of Denmark, Elektrovej, bygn. 327, 2800 Kgs. Lyngby (Denmark)
[3]European Space Agency, ESTEC, Keplerlaan 1, 2201 AZ Noordwjik (The Netherlands)
[4]DTU Fysik, Techn. Univ. of Denmark, Fysikvej, bygn. 311, 2800 Kgs. Lyngby (Denmark)
[5]Politecnico di Milano, Via La Masa 1, 20156 Milano (Italy)

## ABSTRACT

The ATHENA X-ray observatory is a large-class ESA approved mission, with launch scheduled in 2028. The technology of silicon pore optics (SPO) was selected as baseline to assemble ATHENA's optic with more than 1000 mirror modules, obtained by stacking wedged and ribbed silicon wafer plates onto silicon mandrels to form the Wolter-I configuration. Even if the current baseline design fulfills the required effective area of 2 $m^2$ at 1 keV on-axis, alternative design solutions, e.g., privileging the field of view or the off-axis angular resolution, are also possible. Moreover, the stringent requirement of a 5 arcsec HEW angular resolution at 1 keV entails very small profile errors and excellent surface smoothness, as well as a precise alignment of the 1000 mirror modules to avoid imaging degradation and effective area loss. Finally, the stray light issue has to be kept under control. In this paper we show the preliminary results of simulations of optical systems based on SPO for the ATHENA X-ray telescope, from pore to telescope level, carried out at INAF/OAB and DTU Space under ESA contract. We show ray-tracing results, including assessment of the misalignments of mirror modules and the impact of stray light. We also deal with a detailed description of diffractive effects expected in an SPO module from UV light, where the aperture diffraction prevails, to X-rays where the surface diffraction plays a major role. Finally, we analyze the results of X-ray tests performed at the BESSY synchrotron, we compare them with surface finishing measurements, and we estimate the expected HEW degradation caused by the X-ray scattering.

**Keywords:** ATHENA, silicon pore optics, design, simulation, modeling

## 1. INTRODUCTION

With a 12 m focal length, an angular resolution below 5 arcsec half-energy width (HEW), an effective area of at least 2 $m^2$ at 1 keV and 0.25 $m^2$ at 6 keV, the ATHENA X-ray telescope[1] will be the largest X-ray observatory ever built. The project is already approved by ESA with a launch scheduled in 2028, and the technology needed to reach these tight specifications is currently under study. Since 2004, the technology of silicon pore optics (SPO) is being developed at ESTEC to solve the problem of manufacturing lightweight, segmented, and focusing optics with the mentioned effective area and angular resolution values. SPO mirror modules (MM), currently manufactured at the Cosine company (Warmond, The Netherlands), consist of stacks of wedged and grooved silicon wafers with excellent surface smoothness and thickness uniformity. The grooved silicon plates are stacked onto silicon mandrels that endow them with the required curvature in both directions, and the adhesion of plates is ensured by Van der Waals interactions acting between the accurately polished surfaces when they come into contact.[2] The longitudinal curvature can be parabolic or hyperbolic; therefore, aligning a parabolic and a hyperbolic MM (Fig. 1a) one reconstitutes the Wolter-I[3] focusing geometry, widespread in astronomical X-ray optics. One of the advantages of this approach is that silicon plates with high uniformity and smoothness – typically required to minimize figure errors and surface roughness – are already available in the semiconductor market at an affordable cost. Moreover, monocrystalline silicon has a very high thermal conductivity, suitable to minimize thermal gradients in space operation.

e-mail: daniele.spiga@brera.inaf.it, phone: +39-02-72320427

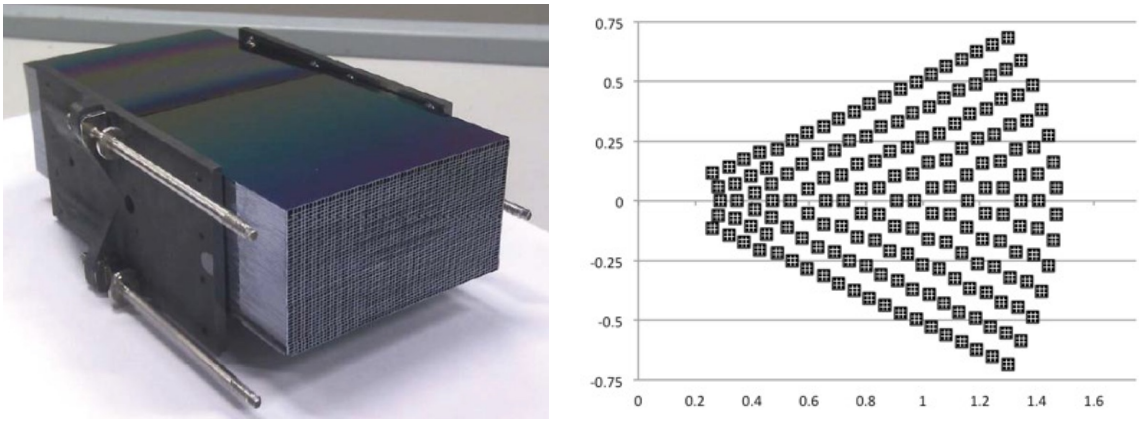


a) b)

Figure 1. a) A Wolter-I SPO mirror module (image credits: ESA) is made of a double stack made of silicon plate pairs, one with parabolic and the other with hyperbolic longitudinal profiles. Typical pore pitch values are 1 to 3 mm, while the pore height is 0.606 mm. The mirror membrane is 0.17 mm thick, while the rib width can be constant (also 0.17 mm thick) or, for the inner mirror modules, variable along the plate width to ensure the radial alignment of ribs.[4] b) Graphic representation of the mirror modules positions in one of the six petals composing the ATHENA optics.

The production of more than 1000 flight-grade MMs and the subsequent integration and alignment into the ATHENA petal structure clearly require a preliminary simulation of the achievable optical performances. This paper shows the first results obtained by the ESA-supported SImPOSIUM (*SIlicon Pore Optics SImUlation and Modelling*) collaboration between INAF-OAB and DTU Space to elaborate algorithms and pieces of software for simulation of SPO performances under different aspects. An important activity is devoted to the design of the optics, from pore to telescope level. In fact, a baseline design for the ATHENA telescope has been provided by ESA and proved to fulfill the on-axis effective area requirements, but alternative designs may exist, e.g., privileging the field of view (wider rib and plate spacings) at the expense of some reduction of the on-axis area, or the adoption of polynomial profiles[5] to replace the Wolter's, so to limit off-axis aberrations. The methodology we are adopting, for now limited to the effective area modeling, is described in Sect. 2.

The performance prediction of a given optical design is a typical problem of geometric optics. If diffractive effects can be neglected at the first order, the effective area and the point spread function (PSF) can be simulated using *ray-tracing* methods, possibly accounting some correction for the X-ray scattering caused by the surface roughness. To this end, the scattering diagram can be modeled from the measured roughness and be used to alter the reflection process in the ray-tracing simulator. In this project, the McXtrace package[6] has been used to implement the complex structure of the ATHENA optics. Section 3.1 reports an overview of the results, while the complete McXtrace simulation is described with more detail in another paper of this volume.[7] In order to determine the accuracy needed to align more than 1000 MMs into the petal structure, ray-tracing methods are also implemented to simulate the effects of MM misalignments on the optical performances (Sect. 3.2), using a specific code written in MATLAB language. Another code (MT_RAYOR) is adopted[8] to obtain the first simulations of stray light in the ATHENA optical assembly (Sect. 3.3).

Diffractive effects in an obstructed aperture like SPO's deserve a detailed treatment (Sect. 4). The pores are $10^6$ times larger than the typical $\lambda$ values for X-rays, making the aperture diffraction almost negligible[9] and thereby justifying the ray-tracing approach adopted in Sects. 2 and 3. However, UV illumination is often used to co-focally align assemblies of SPO MMs, and the aperture diffraction become predominant in this range of $\lambda$ values. In contrast, diffraction effects typically arise in X-rays from surface microroughness;[10] even if silicon wafers are characterized by an excellent surface smoothness, the tight requirements of ATHENA (HEW $<$ 5 arcsec at 1 keV and HEW $<$ 10 arcsec at 6 keV) require to precisely specify a roughness tolerance in terms of power spectral density (PSD). In Sect. 5, X-ray scattering measurements taken at the PTB laboratory of the BESSY synchrotron facility[11] are used to derive the coating interface PSD, which is compared with experimental topographic data taken on coated silicon plates, and used to evaluate the HEW degradation with increasing energy caused by scattering.

Finally, we show (Sect. 6) the first steps taken in the simulation of a magnetic diverter for ATHENA, aiming at deflecting charged particles out of the detector field, based on a simple arrangement of permanent magnets.

## 2. ANALYTICAL MODELING OF THE EFFECTIVE AREA

The design of an effective focusing system for the ATHENA telescope within the current constraints (3 m to 0.55 m mirror diameters and 12 m focal length) is a crucial point. At the time of writing, ESA's reference design[12] is based on 20 rows of SPO MM with increasing curvature radii, and with MMs based on the Wolter-I geometry, fixed pore width and height, plate lengths varying in inverse proportion with the incidence angle to maximise the effective area on-axis. The geometric design, together with the adoption of a proper reflective coating (an $Ir/B_4C$ bilayer), fulfills the on-axis effective area requirements of 2 $m^2$ at 1 keV and 0.25 $m^2$ at 6 keV.

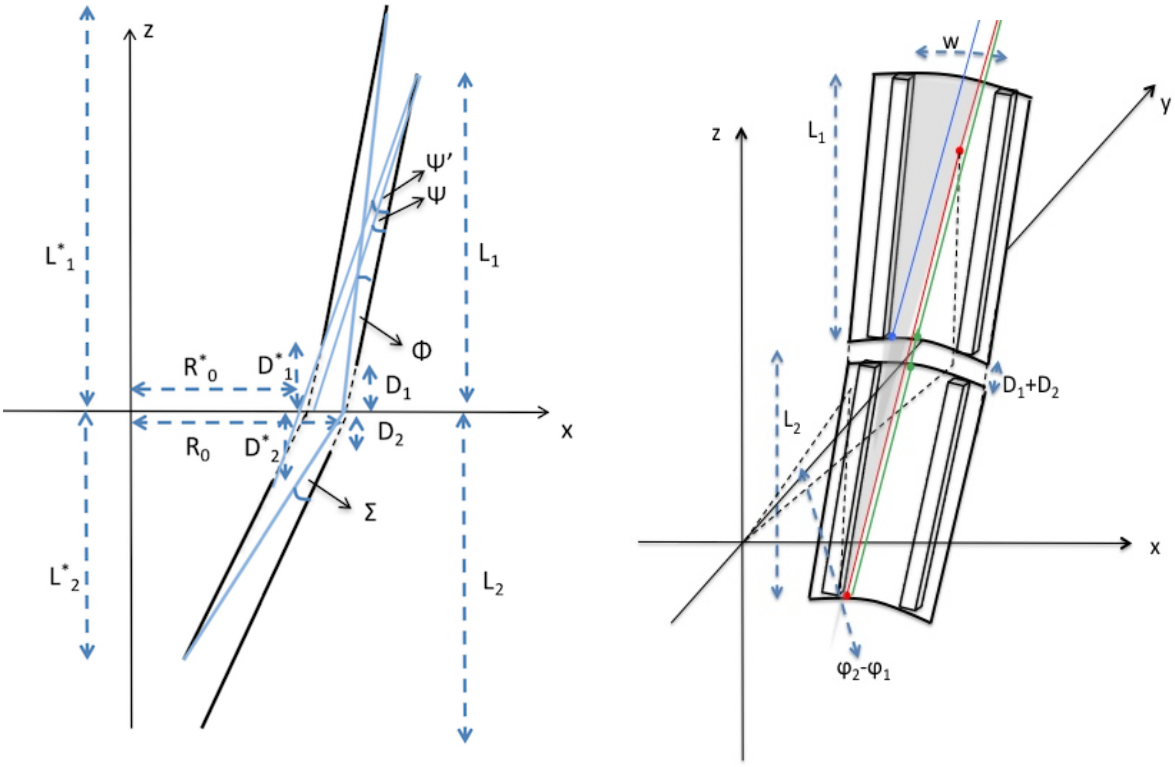


a) b)

Figure 2. a) Radial section of a pore in a generic configuration of variable plate length. The obstruction parameters[13] $\Phi$, $\Psi$, and $\Sigma$ are shown. b) Off-axis obstruction by ribs (membrane thickness and rib heights are not to scale). Rays can be blocked before the first reflection (blue), between the two reflections (red), or after the second reflection (green). We have drawn only the last obstructed ray.

However, better solutions in terms of throughput or angular resolution might in principle exist: changes in the general constraints may intervene in the mission developments, such as variations of the maximum diameter or the focal length. In this occurrence, the optical design has to be completely changed. Providing an effective design of a large optical system using a number of SPO MMs is in principle a complex problem, involving a huge number of variables. Moreover, the performance verification of a given configuration, when achieved by means of ray-tracing methods, is in general time consuming and a selection of the most performing configuration requires iterating the routine several times. Fortunately, owing to the overwhelmingly long focal length in use in comparison to the mirror plate lengths, the computation of the effective area can be greatly simplified. In fact, the longitudinal profile sag is so small that even a double cone approximation can be adopted to compute the effective area. On the other hand, the choice of the longitudinal profile type (e.g. Wolter-I[3] or polynomial[5])

can be tuned on the basis of the tolerable off-axis aberration within the field of view almost regardless of the geometrical dimensions (lengths, angles, radii) of the mirror plates.[13]

At this stage, we have determined the analytical expression for the vignetting factors of a pore in the radial and the azimuthal directions. In fact, SPOs are naturally discretized in the spatial occupancy of the aperture pupil, hence we can consider the incidence angles on the primary and the secondary surfaces, $\alpha_1$ and $\alpha_2$, fairly constant within a single pore. So we can also assume constant in a pore the respective reflectivity values, $r_\lambda(\alpha_1)$ and $r_\lambda(\alpha_2)$, as functions of the X-ray wavelength $\lambda$. This fact allows us to instantly compute the effective area of a mirror module without statistical uncertainties.

We consider a double reflection pore (Fig. 2a) of azimuthal width $w$ and radial height $h$. The reflective plate pair has azimuthal curvature radius $R_0$, focal length $f$, length of the primary segment $L_1$, length of the secondary segment $L_2$, including the respective gaps at the intersection plane, $D_1$ and $D_2$. The mirror surface is obstructed by the next inner silicon plate pair, whose respective parameters are marked with a "*" superscript. The expression of the effective area of the reflective pair, if continuous at the intersection plane, for an infinitely distant source, off-axis by an angle $\theta \geq 0$, and in absence of rib obstructions, would be provided by the usual formula:[13]

$$A_\infty(\lambda,\theta) = R_0 \int_{\varphi'}^{\varphi''} [(L\alpha)_{\min} - O_{\max}]_{\geq 0}\, r_\lambda(\alpha_1)\, r_\lambda(\alpha_2)\, \mathrm{d}\varphi, \tag{1}$$

where the polar angle $\varphi$ is measured from the off-axis plane and varies from $\varphi'$ to $\varphi''$. The brackets $[\ ]_{\geq 0}$ mean that the enclosed expression is to be set to 0 when negative. The expressions appearing in the integrand are

$$(L\alpha)_{\min} = \min(L_1\alpha_1, L_2\alpha_2, L_1\Psi), \tag{2}$$

$$O_{\max} = \max[L_1^*(\alpha_1 - \Phi), L_2^*(\alpha_2 - \Sigma), 0], \tag{3}$$

which are functions of $\varphi$ via the expressions of the incidence angles:[14]

$$\alpha_1 = \alpha_0 - \theta\cos\varphi, \tag{4}$$

$$\alpha_2 = \alpha_0 + \theta\cos\varphi. \tag{5}$$

In Eq. 2 and 3, the three obstruction parameters $\Phi$, $\Psi$, and $\Sigma$ (Fig. 2a) determine the obstruction of rays before the first reflection, after the first reflection, and after the second reflection respectively (see[13] for further details).

In Eq. 1 we still have to account for the gaps at the intersection plane. To this end, we notice that Eq. 2 describes the obstructions near the entrance pupil and Eq. 3 the obstructions near the intersection plane. Since the gaps contribute to the latter, to account for the related loss of effective area we just have to modify Eqs. 2 and 3 as follows:[15]

$$(L\alpha)'_{\min} = \min(L_1\alpha_1, L_2\alpha_2, L_1\Psi'), \tag{6}$$

$$O'_{\max} = \max[L_1^*(\alpha_1 - \Phi), L_2^*(\alpha_2 - \Sigma), D_1\alpha_1, D_2\alpha_2, 0]. \tag{7}$$

In Eq. 6, the $\Psi$ parameter has been modified to account for the reduced obstruction at the intersection plane:

$$\Psi' = \Psi + \alpha_0^* \frac{\min(D_1^*, 3D_2^*)}{L_1}. \tag{8}$$

From Eqs. 6 and 7 we obtain the effective area of the mirror plate pair with gaps at the intersection plane:

$$A_\infty(\lambda,\theta) = R_0 \int_{\varphi'}^{\varphi''} [(L\alpha)'_{\min} - O'_{\max}]_{\geq 0}\, r_\lambda(\alpha_1)\, r_\lambda(\alpha_2)\, \mathrm{d}\varphi. \tag{9}$$

We finally have to account for the off-axis obstruction caused by the ribs (Fig. 2b). An approximate expression for the rib vignetting factor is

$$V_{\mathrm{R}}(\varphi) = 1 - \frac{\theta\,|\sin\varphi|}{w}(L_1 + L_2), \tag{10}$$

provided that it is non-negative (a derivation of this formula is reported elsewhere[15]). Within a single pore, $\varphi$, $\alpha_1$, and $\alpha_2$ can be considered constant and Eq. 9 can be simplified:

$$A_{\rm pore}(\lambda,\theta) = wV_{\rm R}[(L\alpha)'_{\rm min} - O'_{\rm max}]_{\geq 0}\, r_\lambda(\alpha_1)\, r_\lambda(\alpha_2). \tag{11}$$

In the last passage we used the relation $w = R_0(\varphi'' - \varphi')$, which is another constant characteristic of the MM, and we have accounted for the rib obstruction described by Eq. 10.

In the current design of the ATHENA telescope, with excellent approximation, we have $L_1^* = L_2^* = L_1 = L_2 := L$, $D_1^* = D_2^* = D_1 = D_2 := D$. In addition, $f \gg L$, and this entails $\Phi \approx \Psi \approx \Sigma$. Moreover, the filling factor of the pores is 1 to a very good approximation. This means that the reflective surface of the pore at $z = +L$ has the same radial coordinate of the non-reflective surface at $z = +D$. This is exactly fulfilled for the central plate in the module, and only approximately for the others because the incidence angle gradually varies in the stack. We can therefore write $h \simeq (L - D)\alpha_0$, and the obstruction parameters become

$$\Phi \approx \Sigma \approx \Psi \approx \frac{h}{L} \simeq \alpha_0(1-\xi), \tag{12}$$

having defined $\xi = D/L$. In practice, we always have $\xi \ll 1$.

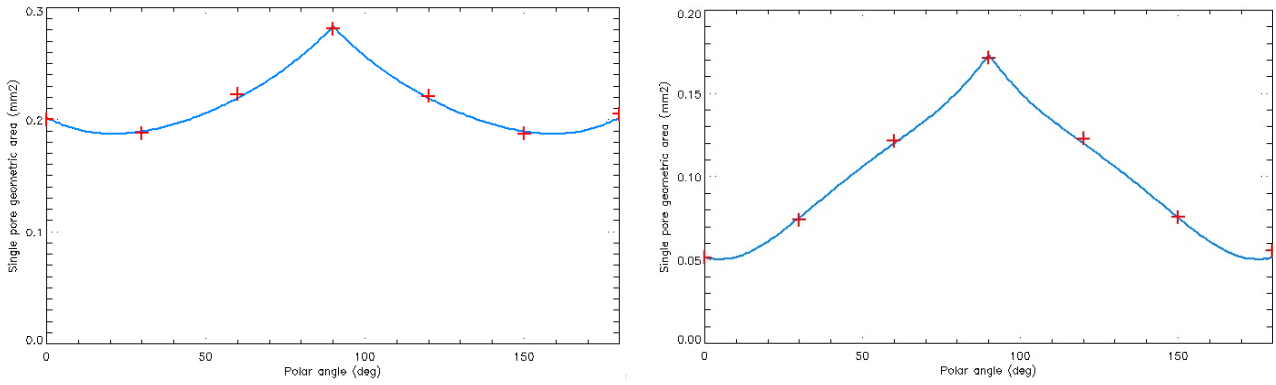


a) b)

Figure 3. Pore geometric area for $L_1 = L_2 = 31$ mm, $D_1 = D_2 = 2$ mm, $w = 1$ mm, $h = 0.6$ mm, $\alpha_0 = 1.2$ deg and variable $\varphi$. Blue line: analytical result. Red crosses: ray tracing results. a) $\theta = 20$ arcmin. b) $\theta = 30$ arcmin.

We now compute the effective area of the single pore: using Eqs. 4, 5, and 12, we obtain $\alpha_1 - \Phi \approx \xi\alpha_0 - \theta\cos\varphi$ and $\alpha_2 - \Sigma \approx \xi\alpha_0 + \theta\cos\varphi$. Moreover, $\Psi$ should be replaced by $\Psi'$ (Eq. 8), which in the present case ($D_1 = D_2$) takes the form $\Psi + \xi\alpha_0^*$, i.e. (Eq. 12), $\Psi' \simeq \alpha_0$. Putting all this into Eqs. 6, 7, and 11, we remain with

$$A_{\rm pore}(\lambda,\theta) = wLV_{\rm R}[\min(\alpha_1,\alpha_2,\alpha_0) - \max(\xi\alpha_0 - \theta\cos\varphi, \xi\alpha_0 + \theta\cos\varphi, \xi\alpha_1, \xi\alpha_2)]_{\geq 0}\, r_\lambda(\alpha_1)\, r_\lambda(\alpha_2). \tag{13}$$

As $\min(\alpha_1,\alpha_2) = \alpha_0 - \theta|\cos\varphi| \leq \alpha_0$, and substituting Eqs. 4 and 5, we can simplify Eq. 13 as follows:

$$A_{\rm pore}(\lambda,\theta) = wLV_{\rm R}\left[\alpha_0 - \theta|\cos\varphi| - \xi\alpha_0 - \max\left(\theta|\cos\varphi|, \xi\theta|\cos\varphi|\right)\right]_{\geq 0}\, r_\lambda(\alpha_1)\, r_\lambda(\alpha_2), \tag{14}$$

where $\xi\alpha_0$ was moved out of the max operator. As $\xi \ll 1$, we have

$$A_{\rm pore}(\lambda,\theta) = wLV_{\rm R}\left[(1-\xi)\alpha_0 - 2\theta|\cos\varphi|\right]_{\geq 0}\, r_\lambda(\alpha_1)\, r_\lambda(\alpha_2), \tag{15}$$

where we see that in the current configuration the nesting obstruction completely supersedes the effect of the gaps. Finally, replacing the expression of Eq. 10 into Eq. 15, we remain with

$$A_{\rm pore}(\lambda,\theta) = \underbrace{[w - 2L\theta\,|\sin\varphi|]_{\geq 0}}_{\text{azim. vign.}}\,\underbrace{[(L-D)\alpha_0 - 2\theta L\,|\cos\varphi|]_{\geq 0}}_{\text{radial vignetting}}\, r_\lambda(\alpha_1)\, r_\lambda(\alpha_2). \tag{16}$$

We could also check the correctness of Eq. 16 by running a detailed ray-tracing routine on a single pore, accounting for the single-reflections losses, the obstructions by non-reflective sides, and including the absorption on the lateral walls of the ribs. The agreement of the geometric areas (i.e., assuming $r_\lambda(\alpha) = 1$) is excellent, as shown in Fig. 3.

We finally note that Eq. 16 is valid only if the two stacks have equal lengths, the same intersection plane, and a filling factor exactly equal to 1 as in the reference design. In all the other cases, the more general Eq. 11 should be used. The next step will be the writing of the analytical expression for the total effective area of ATHENA optics, and the subsequent parameter optimization for a figure of merit to be selected.

## 3. GEOMETRIC OPTICS SIMULATIONS

### 3.1 Ray-tracing simulations using McXtrace

Ray tracing simulations are performed at DTU Space using *McXtrace*, freely distributed and open source software for simulating X-ray instruments.[6] Doing this, we have taken advantage of the available database of X-ray elements already included in the McXtrace package to build a ray tracing model of the ATHENA optics.

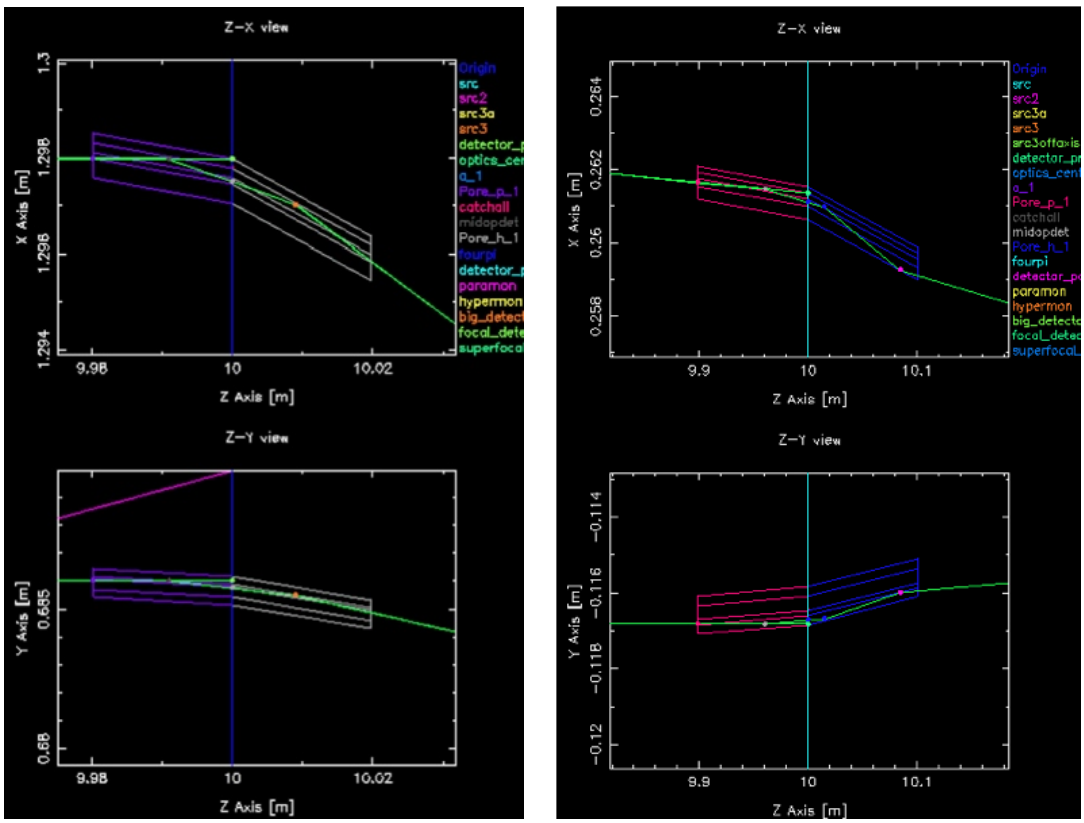


a) b)

Figure 4. On-axis (a) and 10 arcmin off-axis (b) traced ray simulated with McXtrace. We note how the off-axis ray ends up hitting the bottom surface of the hyperbolic pore.

We have so far implemented the baseline geometry[12] and mirror coatings provided by ESA, a Wolter-I X-ray optic with SPO mirrors coated with an Ir/$B_4C$ bilayer (10 nm of Ir plus 8 nm of $B_4C$). As the optimization of the geometry of the optics evolves (Sect. 2) we will implement and simulate alternative design geometries.

An illustration of the geometry of ATHENA optics simulated in this task is shown in Fig. 1b. Ray-tracing with McXtrace is done on individual pore level (Fig. 4) and allows for evolution to a single SPO mirror plate, mirror modules and the complete ATHENA optic. Using ESA's reference design as input, we have simulated X-rays traveling through one set of pores (parabolic and hyperbolic) for each mirror module within one petal.

That means that for each of the 177 mirror modules, we traced the central pore of the module and assumed that the results for that one central pore is representative of the performance of the given mirror module. A flawless profile is also assumed. Some variables can be provided as input parameters:

- pore width and height,
- rib width,
- wafer thickness,
- membrane thickness,
- SPO plate width,
- SPO length,
- height of mirror modules,
- mirror module number per ring,
- position of mirror module within the optics,
- mid radius of mirror modules,
- parabolic radius and hyperbolic radius for each set of SPOs,
- telescope focal length,
- $Ir/B_4C$ bilayer coating,
- surface roughness.

Finally, we have assumed converging ribs of the SPO plates.

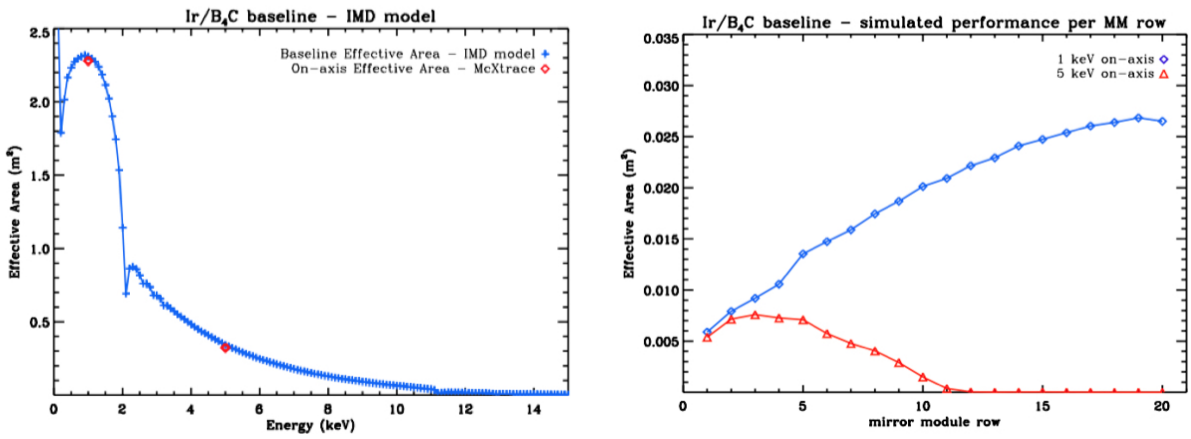


a) b)

Figure 5. a) On-axis effective area theoretical model (line) along with the simulated effective areas (symbols) at 1 keV and 5 keV. b) Simulated effective area per mirror module row at 1 keV and 5 keV.

We have evaluated the performance of the pores by ray tracing at two standard energies, 1 keV and 5 keV. Preliminary results include simulated on-axis effective area (Fig. 5a) and performance per mirror module within the petal (Fig. 5b). Moreover, in Fig. 5a we compare the simulated on-axis effective areas at 1 keV and 5 keV with the theoretical model computed using the software IMD,[16] considering the same pore geometry and mirror coatings. The agreement is excellent. More results, such as the computed effective area off-axis, are reported in detail in another paper of this volume.[7]

To date, we have a working set of models on a pore level for the true Wolter-I ATHENA optic. We have tested the models for arbitrary position of pores/modules, specified as an input file and for the present baseline coating designs. The return number of in-pore reflections for the simulations performed does match well the on-axis theoretical models and seem to be a very accurate simulation of the expected geometry of the telescope. The models allow for reflection on all four walls of a pore, but at the present time we have only considered reflections only on the coated surface. Moreover, the pore-level models are currently unable to provide information on cross-talk between pores and the possibility of implementation of cross-talk on mirror module level will be evaluated.

### 3.2 Simulating misalignments in mirror modules

In order to ensure a final HEW below 5 arcsec at 1 keV, not only the individual MMs need an angular resolution better than 5 arcsec: part of the error budget is allocated to alignment errors. Misalignments are responsible, in fact, for effective area loss, HEW degradation, and focal spot displacements. In this section we carry out an analysis of the sensitivity to the roto-translation errors at MM level, to be later implemented at the level of the entire ATHENA optics. The effects are evaluated trough ray-tracing simulations based on the standard MonteCarlo approach and written in MATLAB code. For each ring, the MM corresponding to the polar angle $\varphi = 0$ is considered as a test case. A 0.17 mm rib thickness and a 3 mm rib spacing is assumed.

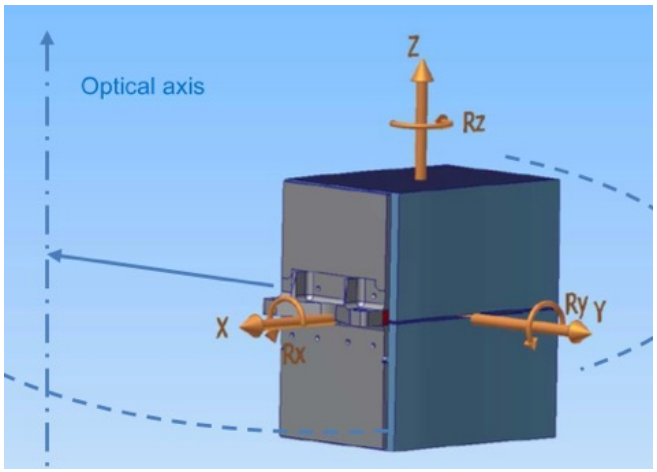


Figure 6. The reference frame in use in the following definitions of the misalignments/displacements (image credits: Media-Lario Technologies).

After imparting a roto-translation to the module according to the axis orientation drawn in Fig. 6, a number of rays is launched and their path through the modules is analyzed to find the arrival position on the focal plane to determine the barycenter of the focal spot, the HEW of the focal spot, and vignetting effects.

The rays are uniformly generated just above the entrance of the MM aperture, in this case parallel to the $z$-axis. Their paths are followed up to the MM exit to check the geometrical vignetting of the different structures (back surface of plates or ribs). The impact position of the plate surfaces is determined as the intersection of 3D polynomial surfaces, axially symmetric, with the ray. These surfaces can be reduced to the conventional parabolic and hyperbolic surfaces selecting the correct values of the polynomial coefficients, but are already defined in the most generic way to guarantee the maximum flexibility in view of a possible optical design optimization. The solution of the equation provides the coordinates of the incidence point.

Passing through the module, the rays on the optical surface of the plates follow geometrical optics. It is already possible for a surface figure error to be taken into account in the reflection: depending on the hitting position of the plate surface, the local surface orientation may be altered according to either a tabulated error map or/and a random error with an assigned distribution. It is likewise possible to add a simplified scattering model. The reflectivity of the surface is computed using the standard Fresnel equations.

When a set of roto-translation parameters (translations along $x, y, z$ and rotations about the same axes, see Fig. 6) for each MM type is provided within a specified range of values, the effect of the MM misalignment is treated as a simple change of reference frame. In the future developments of this work, the initial position and direction of the incoming rays, the final position and directions after the reflections will be conveniently modified by means of the quaternion algebra, which provides a fast and reliable way to represent roto-translations in 3D space. Using the code described above, the sensitivity analysis has been carried out based on ESA's reference design[12] with the plates of the MMs in their nominal Wolter-I configuration, and rings are labeled with 1 to 20 going toward the largest radii. The results can be summarized as follows.

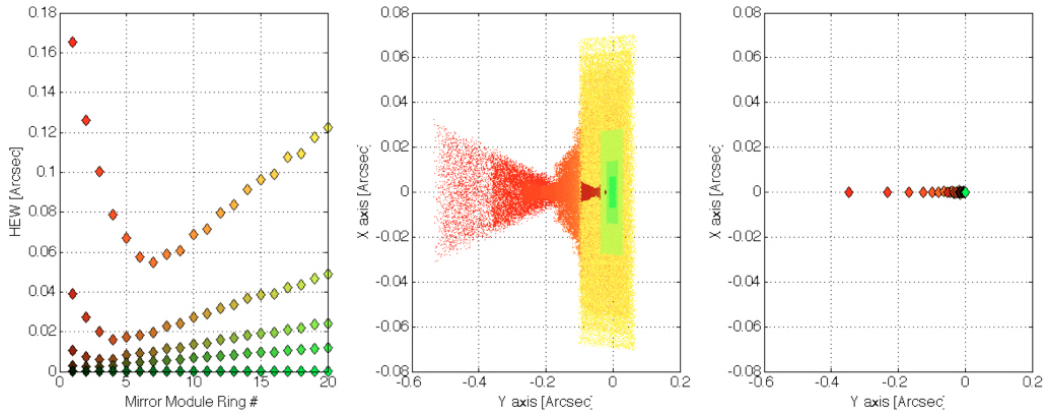


Figure 7. Rotation effects (0, 10, 30, and 60 arcsec) around the $x$-axis for the different MMs. Left: HEW contribution as a function of the rotation angle. Middle: focal spot images depending on rotation angle. Right: barycenter position of the focal spot.

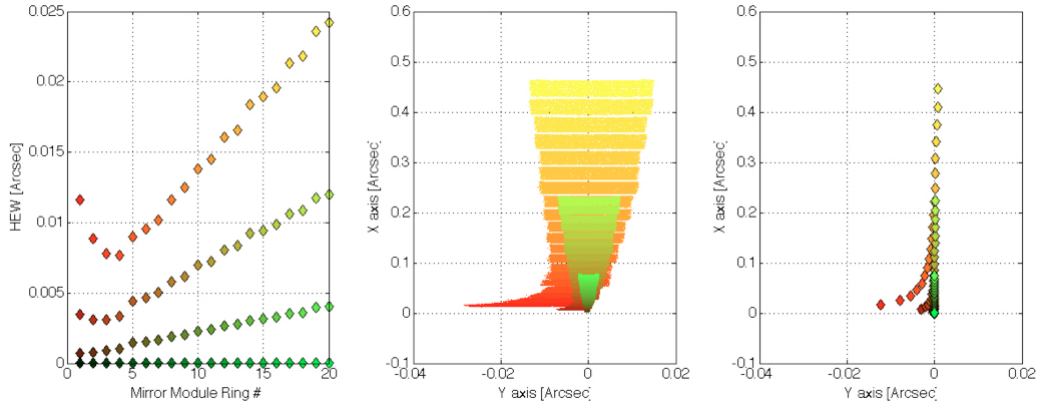


Figure 8. Rotation effects (0, 10, 30, and 60 arcsec) around the $y$-axis for the different MMs. Left: HEW contribution as a function of the rotation angle. Middle: focal spot images depending on rotation angle. Right: barycenter position of the focal spot.

1. Translation errors along the $x$-axis and $y$-axis (i.e., the de-centering of the MM from its nominal position) simply displace the focal spot in the same directions, with an impact equal to the plate scale (17.189 arcsec/mm).
2. Translation errors along the $z$-axis have an impact that depend on the ring. The displacement of the barycenter is between 0.41 arcsec (ring 1) and 2.09 arcsec (ring 20). The displacement is larger for outermost rings: the maximum is found around 2.1 arcsec for ring 20. The intrinsic HEW of the spot caused by defocus is around 0.03 arcsec for the innermost rings (1 to 4), while it amounts to 0.06 arcsec for rings 5 to 20.
3. A rotation around the $x$-axis does not cause a significant increase of the HEW: it rather moves the image barycenter along the $y$-axis. The HEW, the focal spots, and the barycenter location as a function of the ring number, for a set of rotations up to 1 arcmin are shown in Fig. 7. The innermost rings exhibit larger barycenter displacements. A rotation of 1 arcmin, for example, displaces the barycenter along the $y$-axis up to a maximum of 0.35 arcsec for the innermost ring. The intrinsic HEW contribution is from 0.17 arcsec for ring 1, decreases to 0.06 arcsec for ring 4, and eventually increases to 0.12 arcsec for ring 20.
4. Also a rotation around the $y$-axis does not contribute to a relevant increase the HEW, but it moves the image barycenter mostly along the $x$-axis. The HEW, the focal spots, and the barycenter location as a function of the ring number, for a set of rotations up to 1 arcmin are shown in Fig. 8. With a rotation of 30 arcsec, for example, the displacement is in the range 0.012 - 0.223 arcsec, increasing toward the outermost rings. The intrinsic HEW contribution increases from 0.0035 arcsec for ring 1 to 0.012 arcsec for ring 20.

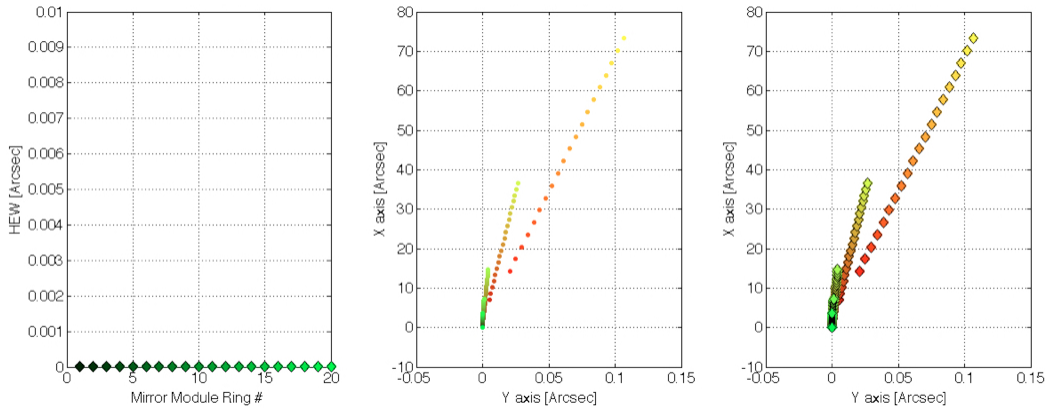


Figure 9. Rotation effects (0 , 30, 60, 120, 300, and 600 arcsec) around the $z$-axis for the different MMs. Left: HEW contribution as a function of the rotation angle. Middle: focal spot images depending on rotation angle. Right: barycenter position of the focal spot.

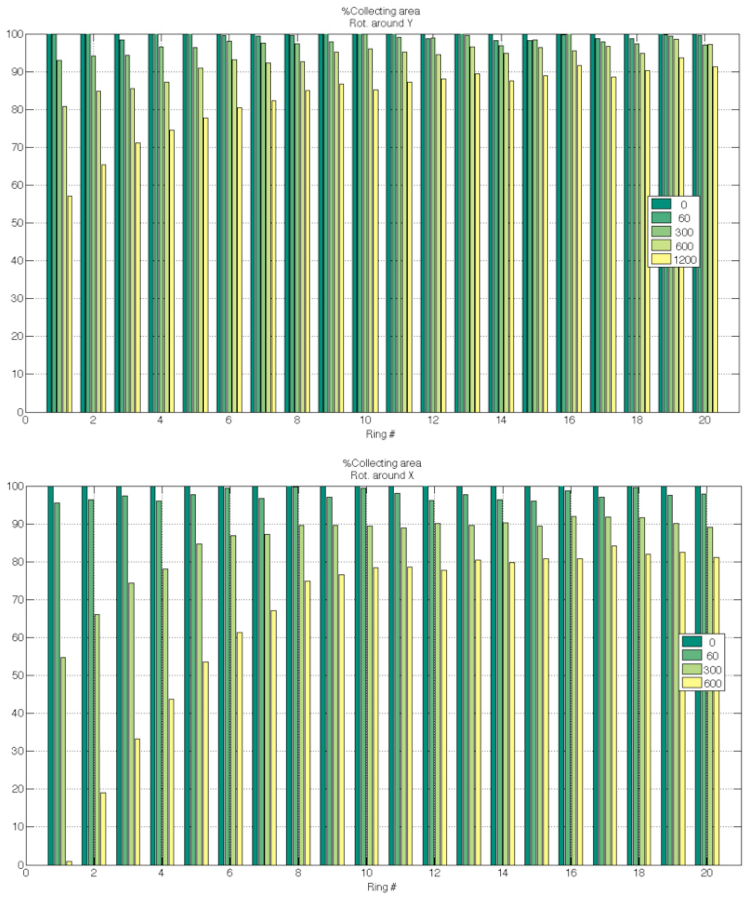


Figure 10. Percent of residual collecting area with respect to the on-axis configuration for different rotation amplitudes (0 ,60, 300, 600, and 1200 arcsec). Top: rotation around $y$-axis. Bottom: rotation around $x$-axis.

5. A rotation around the $z$-axis does not introduce any aberration in the focal spot, but moves the image barycenter mostly along the $x$-axis. The HEW, the focal spots, and the barycenter location as a function of the ring number, for a set of rotations up to 10 arcmin are shown in Fig. 9. For example, a rotation of 60 arcsec displaces the barycenter along the $x$-axis by an angle variable from 13 arcsec (ring 1) to 75 arcsec (ring 20). The intrinsic contribution to the HEW is always zero.

Regarding the sensitivity of the effective area to misalignments, the residual fraction of the effective area for rotations around the $y$-axis is shown in Fig. 10, top. Different rotation amplitude angles (0, 60, 300, 600, and 1200 arcsec) are considered. Owing to their geometrical configuration, the innermost rings are much more obstructed than the outer ones. Anyway, the decrease of the collecting area is near 2-7% for all the rings, with a rotation of 60 arcsec. If the maximum rotation amplitude increases to 300 arcsec, the maximum area loss increases to 20%. Figure 10, bottom, shows the effective area vignetting following rotations around the $x$-axis. In this case, the effect is much larger owing to the more pronounced variation of the incidence angles and the consequent increase of the vignetting in the radial direction (see also Sect. 2). The innermost ring loses almost half of the effective area for rotation of 300 arcsec, while the percent of lost effective area is in the range 2-7% for all the MMs if the rotations angles do not exceed 60 arcsec.

The simulations listed above have been repeated in Wolter-Schwarzschild design, a configuration in which the parabola-hyperbola intersection planes of the central plates in each MM lie upon a sphere of radius equal to the focal length, rather than on a plane. This configuration fulfills the Abbe condition better than a pure Wolter-I and therefore limits the off-axis aberrations. The simulation results for rotations about the $y$- and $z$-axis are in line with the previous ones, while for rotations around the $x$-axis the intrinsic HEW and the barycenter displacement effects are reduced by approximately an order of magnitude.

### 3.3 Simulating stray light with MT_RAYOR

As a precursor to the McXtrace analysis of the ATHENA optics, a ray-tracing stray light analysis had been initiated by using MT_RAYOR, a ray-tracing package[8] developed at DTU Space. The raytracing makes use of a MonteCarlo technique where each ray is followed through the optics and tagged according to its fate i.e. absorption, no reflection, single reflection, or double reflection. The rays with less than two reflections (i.e., singly-reflected or directly passing through the optics) are regarded as stray-light. The MT_RAYOR ray-tracing package has been used, e.g., for an intensive analysis of the NuSTAR calibration and performance, and therefore it is sufficiently adequate for these preliminary investigations. A series of ray-tracing runs were made at an energy of 2 keV, correcting the ray-tracing with a scattering distribution in the shape of a Gaussian function. Even on-axis, a relevant fraction of rays was scattered and missed the second reflection, reaching the focal plane. None of them, however, entered the area of the Wide Field Imager (WFI) detector with a either source on-axis (Fig. 11a) or 20 arcmin off-axis (Fig. 11b). We preliminarily conclude that the stray-light does not contaminate the WFI area, at least for $\theta < 20$ arcmin. The presence of on-axis stray light seems to be a consequence

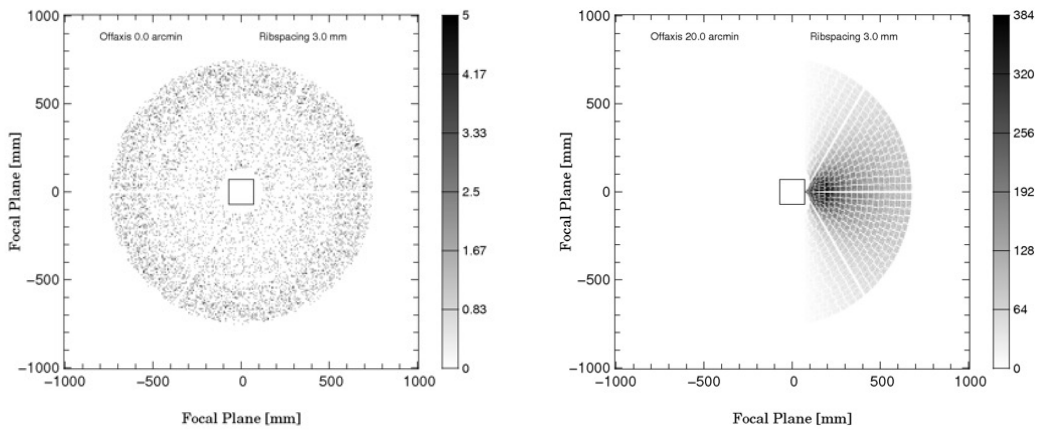


a) b)

Figure 11. The distribution of the stray light rays in the focal plane at 2 keV, as simulated with MT_RAYOR. The central square represents the WFI with a size of 40 arcmin (140 mm). Source a) on-axis, b) 20 arcmin off-axis.

of the assumed scattering model, i.e., a Gaussian, which – being a compact distribution – requires a relevant amplitude to return a HEW value near 5 arcsec, therefore conveying a relevant amount of low-angle scattering. A more realistic model for scattering might be represented by a scattering diagram computed from the measured roughness of SPO samples (Sect. 5.2), and will be implemented in the next phase of this project.

## 4. SIMULATION OF DIFFRACTIVE EFFECTS

Just like conventional X-ray optics, SPOs are also strongly obstructed as a consequence of the dense nesting and the shallow incidence angles. In SPOs, however, also the dense ribbing contributes to obstruct the effective area also on-axis. In X-rays, this essentially results in a reduction of the effective area, with negligible diffraction effects[9] compared to the expected angular resolution that is dominated by the figure errors. In UV illumination, used to locate the focus position in an optical bench, the aperture diffraction becomes largely dominant. On the other hand, diffractive effects are also important in X-rays. While the pore aperture diffraction is usually negligible in X-rays, diffraction off the reflective surface (i.e., the X-ray scattering) becomes important as $\lambda$ decreases, i.e., when the difference of optical paths introduced by the surface roughness starts to be comparable with $\lambda$.

The transition from a situation dominated by aperture diffraction effects (UV) to one chiefly affected by surface diffraction (X-rays) is gradual and a dedicated treatment cannot be devoted to the two spectral ranges. A treatment purely based on physical optics, fortunately, accounts for both effects and even for geometric mirror deformations: the main drawback, however, is that it usually requires a very intensive computation when if considered over a 2D aperture/surface with a sampling of a few microns or less. We have two possible solutions, described in the following sections.

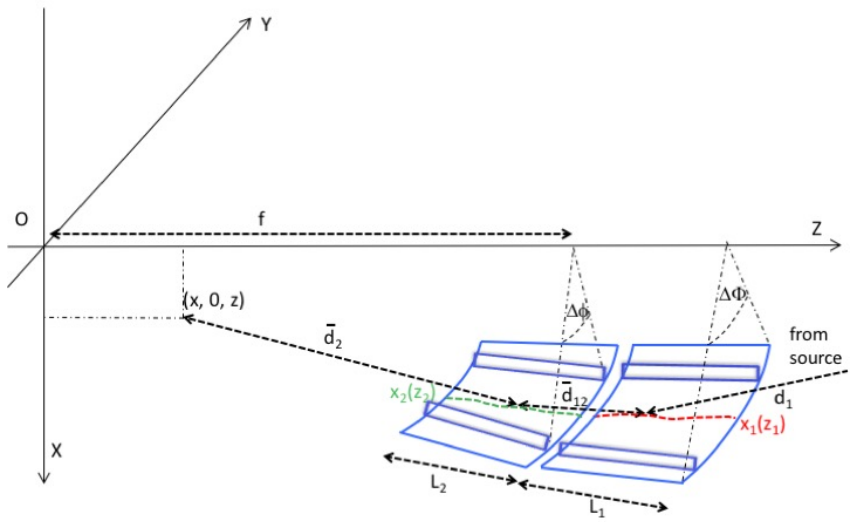


Figure 12. Diffraction in a pore optic, reduced to 1D geometry. The primary segment initially diffracts the incident wavefront to the secondary segment profile. The subsequent diffraction to the focal plane returns the PSF.

### 4.1 Reduction to 1D geometry

In grazing incidence optics, the PSF of a mirror segment is concentrated in the incidence plane. Also the PSF is almost completely affected by longitudinal profiles and only to a minor extent by out-of-roundness errors. Hence, for most applications in X-ray optics the computation can be easily reduced in complexity assuming that the PSF is a variable of the sole $x$ coordinate and determined only by 1D profiles. This case of PSF computation was extensively treated in previous papers[17,18] for the case of integral or segmented grazing-incidence optics, in single or double reflection, near- or far-field approximation, and regardless of the value of $\lambda$. For the SPO case we are considering, the tight ribbing in the azimuthal direction has to be taken into account. In absence of ribs, the electric field from a source on-axis at infinite distance, diffracted to the secondary reflective surface, would be (see[18] with some changes of notation):

$$E_2(x_2, z_2) = \frac{E_0\,\Delta R_1}{L_1\lambda}\int_f^{f+L_1} \mathrm{d}z_1\,\frac{x_1}{\bar{d}_{12}}\,e^{-\frac{2\pi\mathrm{i}}{\lambda}\left(\bar{d}_{12}-z_1\right)}\int_{-\frac{\Delta\Phi}{2}}^{+\frac{\Delta\Phi}{2}}\mathrm{d}\varphi_1\;e^{-\mathrm{i}\frac{\pi x_2\,x_1}{\bar{d}_{12}\lambda}\varphi_1^2}, \tag{17}$$

where (see Fig. 12 and Sect. 2 for the meaning of the symbols) $\varphi_1$ is the polar angle on the primary segment, $\Delta\Phi$ is the azimuthal aperture of the plate, $w$ the pore width, $\Delta\phi = w/R_0$ the azimuthal aperture of a pore, $\Delta R_1 = L_1\alpha_1$, $z_1$ and $z_2$ the axial coordinates of the primary and the secondary mirror surface, $z = 0$ is the nominal focal plane, $x_1(z_1)$ and $x_2(z_2)$ the radial coordinates of the primary and the secondary silicon plate in the $xz$ plane, including figure errors and also the microroughness. The distance $\bar{d}_{12}$ has the expression

$$\bar{d}_{12} = \sqrt{(x_1 - x_2)^2 + (z_1 - z_2)^2}. \tag{18}$$

Since the primary-secondary gap is always very small, we can assume for *not too large* values of $\lambda$ that every single pore of the secondary stack of the MM takes contributions only from the corresponding pore of the primary stack. We can therefore replace $\Delta\Phi$ with $\Delta\phi$ and, setting $\zeta = \varphi_1\sqrt{x_2 x_1/\bar{d}_{12}\lambda}$, rewrite Eq. 17 as

$$E_2(x_2, z_2) = \frac{E_0\,\Delta R_1}{L_1\sqrt{x_2\lambda}}\int_f^{f+L_1} \mathrm{d}z_1\,\sqrt{\frac{x_1}{\bar{d}_{12}}}\,e^{-\frac{2\pi\mathrm{i}}{\lambda}\left(\bar{d}_{12}-z_1\right)}\int_{-\frac{w}{2\sqrt{\bar{d}_{12}\lambda}}}^{+\frac{w}{2\sqrt{\bar{d}_{12}\lambda}}}\mathrm{d}\zeta\;e^{-\mathrm{i}\pi\zeta^2}, \tag{19}$$

having approximated $x_2 x_1 \approx R_0^2$ in the integration limits. As long as $\lambda \ll w^2/\bar{d}_{12}$, the limits can be approximated with infinity and the integral in $\zeta$ equals a constant phase term $e^{\mathrm{i}\pi/4}$. Since $\bar{d}_{12} < L_1 + L_2$, this condition is always met if $\lambda \ll w^2/(L_1 + L_2)$. As in the current design $L_1 + L_2 < 20$ cm and $w > 1$ mm, this condition is surely met if $\lambda \ll 5$ $\mu$m, i.e., in visible light, UV, and – clearly – X-rays. We conclude that in near-field conditions and for $\lambda$ sufficiently small the electric field on the secondary pore segment is essentially unaffected by the presence of the ribs. The resulting expression equals the one valid for mirrors without ribs,[18] which can be safely applied also in SPOs.

In the subsequent diffraction to the focal plane, the situation is different: the electric field takes contributions from all the pores of the MM, therefore the amplitude modulation in the azimuthal direction might in principle be relevant and also affect the PSF in 1D geometry. The exact computation of the Fresnel integral is, however, quite lengthy and will be reported in a subsequent paper.

### 4.2 2D geometry, far-field approximation

In the case of ATHENA, the long focal length allows us applying some approximations that reduce the Fresnel integrals to a Fourier transform. Since efficient numerical routines exist to compute the transform, it becomes possible to perform 2D simulations without excessively increasing the computational load, and still accounting for aperture diffraction, figure errors, and microroughness simultaneously. This approach is used, for example, to compute the scattering contribution in Cherenkov telescope mirrors in near-normal incidence.[19]

We first consider a SPO MM with $M \times N$ pores, total width $W$, total height $H$, pore height $h$, pore width $w$, rib thickness $t$, and membrane thickness $\tau$, illuminated on-axis by a collimated and parallel light source at a distance $S$. We denote the azimuthal curvature radii of the plates at the intersection plane with $R_n$, taking on discrete values with the plate index $n = 0, 1, \ldots, N$. To simulate the 2D diffraction pattern of SPO modules, we start from the far-field expression of the PSF in single reflection from a parabolic, grazing-incidence profile[18] (with slight change of notation):

$$\mathrm{PSF}(\theta) = \frac{1}{h\lambda}\left|\int_0^h e^{-\frac{2\pi\mathrm{i}}{\lambda}\,x_{\mathrm{n1}}\theta}\,\mathrm{CPF}(x_{\mathrm{n1}})\,\mathrm{d}x_{\mathrm{n1}}\right|^2. \tag{20}$$

In the previous equation $\theta = x/f$ is the angular distance from the origin of the coordinates (the nominal focus), $L_1$ the profile length along the $z$-axis, $\alpha_n = R_n/2f$ the incidence angle on the plate at the radial coordinate $R_n$, $x_{\mathrm{n1}}$ the nominal profile of the $n$-th plate defined by the parabolic profile $z_1 = a_n x_{\mathrm{n1}}^2 - 1/4a_n$, where $a_n$ is the variable quadratic coefficient, and CPF is the *complex pupil function* that describes the phase shifts described by possible longitudinal profile errors $x_{\mathrm{e1}}$, projected onto the entrance pupil:

$$\mathrm{CPF}(x_{\mathrm{n1}}) = \exp\left(-\frac{2\pi\mathrm{i}}{\lambda}\,2x_{\mathrm{e1}}\sin\alpha_n\right), \tag{21}$$

where $x_{\mathrm{e1}}$ is a function of $x_{\mathrm{n1}}$.

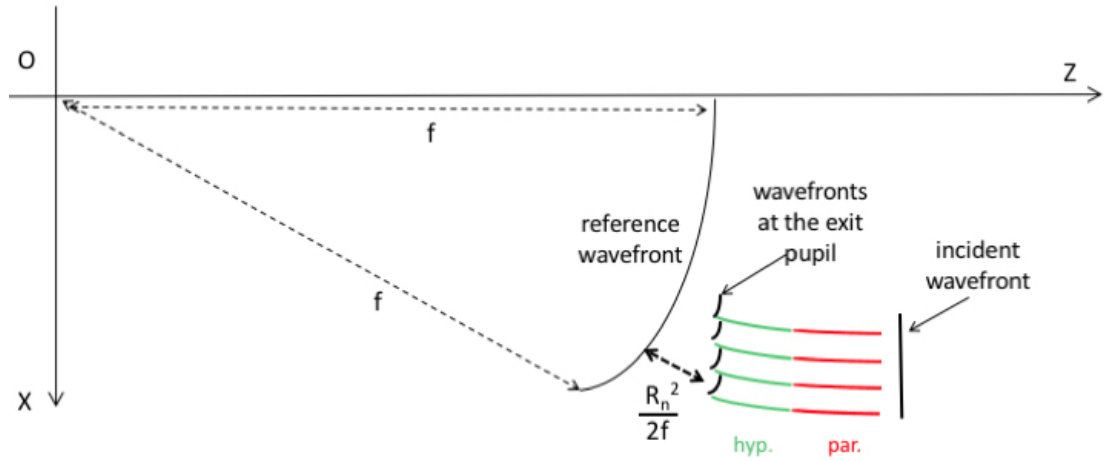


Figure 13. Diffraction from an SPO MM. The diffracted wavefront at the exit pupil consists of a set of spherical wavelets converging to the origin, but with a phase delay increasing with the plate curvature radius.

As diffraction effects caused by the ribs are negligible inside the pore if $\lambda$ is smaller than a few microns (Sect. 4.1), we can assume Eq. 20 to be also valid in the case of a Wolter-I profile, after changing the definition of $\alpha_n = R_n/4f$. For a single pore, the extension of the PSF definition to the 2D case is straightforward,

$$\mathrm{PSF_P}(\underline{r}) = \frac{1}{A_\mathrm{P}\lambda^2 f^2}\left|\int_\mathrm{pore} e^{-\frac{2\pi\mathrm{i}}{f\lambda}(\underline{r}_\mathrm{n1}\cdot\underline{r})}\,\mathrm{CPF}(\underline{r}_\mathrm{n1})\,\mathrm{d}\underline{r}_\mathrm{n1}^2\right|^2, \tag{22}$$

where the PSF is observed at the nominal focal plane and mapped via the coordinates $\underline{r} = (x, y)$. Here $A_\mathrm{P} = h\cdot w$ is the single pore area, mapped by the coordinates $\underline{r}_\mathrm{n1} = (x_\mathrm{n1}, y_\mathrm{n1})$, having selected the origin in the center of the MM entrance pupil, and the CPF now includes the projection of the pore topography on the pupil plane. The extension of Eq. 22 to an azimuthal row of pores in the MM is also immediate as all of them have the same distance from the optical axis, $R_n$, and the same incidence angle, $\alpha_n$:

$$\mathrm{PSF_R}(\underline{r}) = \frac{1}{A_\mathrm{row}\lambda^2 f^2}\left|\int_\mathrm{row} e^{-\frac{2\pi\mathrm{i}}{f\lambda}(\underline{r}_\mathrm{n1}\cdot\underline{r})}\,\chi_\mathrm{P}(\underline{r}_\mathrm{n1})\,\mathrm{CPF}(\underline{r}_\mathrm{n1})\,\mathrm{d}\underline{r}_\mathrm{n1}^2\right|^2, \tag{23}$$

being $\chi_\mathrm{P}$ the characteristic function of the mirror aperture (1 where the reflective surface is present, and 0 elsewhere) and $A_\mathrm{row} = W\cdot h$.

To extend Eq. 23 to a complete SPO stack (Fig. 13), we just have to integrate over the entire mirror module aperture, $A_\mathrm{M}$, accounting for the incidence angle variation resulting from the wedging and the resulting optical path difference[18] between rows, $1/2a_n \simeq R_n^2/2f$,

$$\mathrm{PSF_M}(\underline{r}) = \frac{1}{A_\mathrm{M}\lambda^2 f^2}\left|\int_\mathrm{M} e^{-\frac{2\pi\mathrm{i}}{f\lambda}\left(\underline{r}_1\cdot\underline{r}+\frac{1}{2}R^2\right)}\,\chi_\mathrm{P}(\underline{r}_1)\,\mathrm{CPF}(\underline{r}_1)\,\mathrm{d}\underline{r}_1^2\right|^2, \tag{24}$$

where we defined $A_\mathrm{M} = W\cdot H$ and removed the dependence on the $n$ index, because the transform can now be computed over the aperture pupil of the primary stack (but always keeping in mind that $R$ takes on *discrete* values).

Equation 24 provides the diffraction pattern of the MM in the nominal focus. However, for some applications it can be interesting to simulate the *out-of-focus* diffraction pattern (e.g., at distance $D \neq f$): to this end, one just has to add[20] a fictitious wavefront error $(x_1^2 + y_1^2)(1/2D - 1/2f)$ in order to correct the wavefront curvature at the exit pupil. Therefore, the general expression for the PSF observed at a generic distance $D$ from the module (i.e., at $z = f - D$) is

$$\mathrm{PSF_M^D}(\underline{r}) = \frac{1}{A_\mathrm{M}\lambda^2 D^2}\left|\int_\mathrm{M} e^{-\frac{2\pi\mathrm{i}}{D\lambda}(\underline{r}_1\cdot\underline{r})}\,C(\underline{r}_1)\,\mathrm{d}\underline{r}_1^2\right|^2. \tag{25}$$

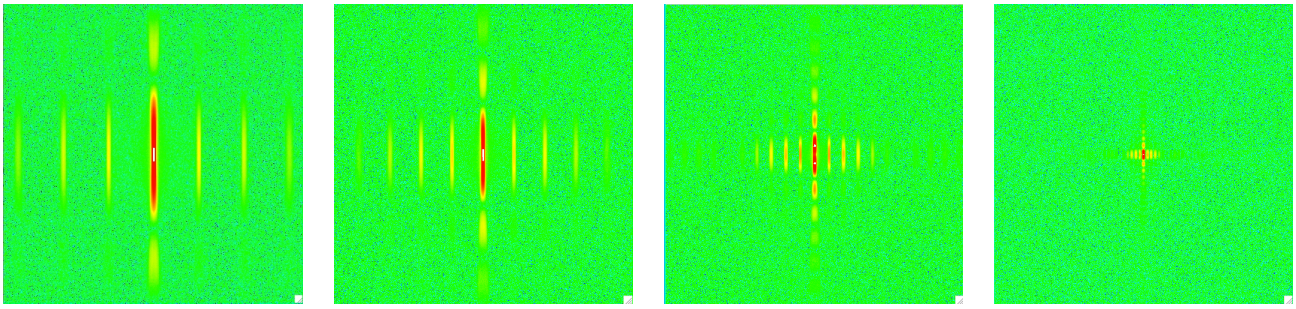

a) b) c) d)

Figure 14. Simulated diffraction patterns of a SPO MM with $f = D = 20$ mm, $w = 0.83$ mm, $h = 0.606$ mm, 34 layers and $W$= 65 mm, at a) $\lambda = 220$ nm, b) $\lambda = 150$ nm, c) $\lambda = 70$ nm, d) $\lambda = 30$ nm. We note the shrinkage of the diffraction figure for decreasing values of $\lambda$. The image field is approximately 30 mm, and the angular diameter of the source is 4 arcsec. The light source is assumed to have a bandwidth $\Delta\lambda$ of a few nanometers.

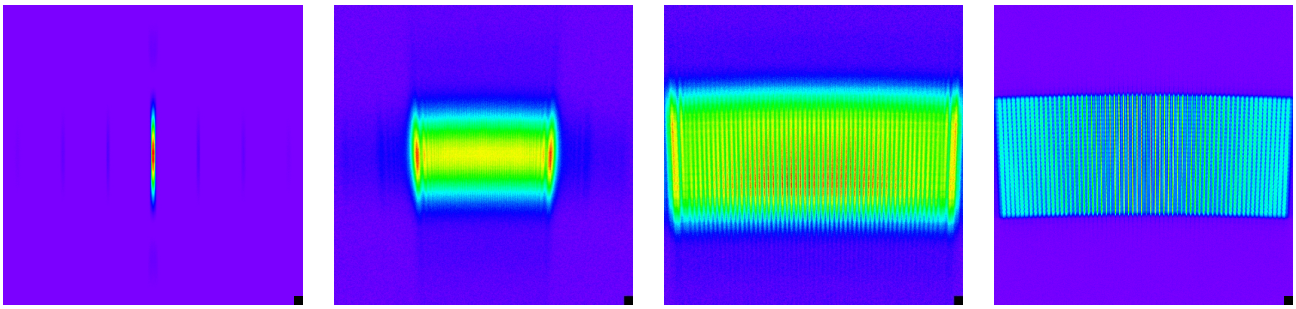

a) b) c) d)

Figure 15. Simulated diffraction patterns of a SPO MM with the same characteristics used in Fig. 14, at $\lambda = 220$ nm, and $f \approx 20$ m. Intra-focus by a) 0 m, b) 4 m, c) 8 m, and d) 16 m (field enlarged by a factor of two). The diffraction figure gradually turns into the image of the SPO aperture for increasing $f - D$ values.

in which we have denoted the generalized pupil function as

$$C(\underline{r}_1) = e^{-\frac{\pi i}{f\lambda}\left[R^2+\left(\frac{f}{D}-1\right)|\underline{r}_1|^2\right]}\,\chi_{\mathrm{P}}(\underline{r}_1)\,\mathrm{CPF}(\underline{r}_1). \tag{26}$$

The last result allows us to overcome one of the limits of the Fraunhofer diffraction, i.e., the evaluation of the diffraction pattern at infinite distance or exactly in focus. Equation 25 enables the simulation also out-of-focus, provided that we remain in the far-field region $D > W^2/4\lambda$. It also reduces the computation to a Fourier transform, for which fast and efficient numerical recipes (FFT) exist. The finite size of the source, if spatially incoherent, can be accounted for in the computation by convolving the PSF out of Eq. 25 with the source demagnified by the ratio $D/S$. Finally, the finite time coherence of the light can be accounted applying Eq. 25 at different values of $\lambda$ within the bandpass $\Delta\lambda$ and averaging the intensity patterns. Because the optical path only varies in the radial direction, the result is equivalent to assume a temporal incoherence of the contributions from different radii. Some examples of application of Eq. 25 are reported in Fig. 14 for variable values of $\lambda$ in the nominal focus, and in Fig. 15 at fixed $\lambda$ and variable intra-focal positions.

In practice, the numerical computation of the Fourier transform in Eq. 25 requires an appropriate definition of the entrance pupil. To ensure proper working of the FFT routine and avoid aliasing problems, one should make sure that:

1. The entrance pupil side, $W_{\mathrm{d}}$, should be twice as large as the maximum size of the SPO MM aperture.[19]
2. The entrance pupil sampling step, $\Delta r_1$, should be at least ten times smaller than $\min(t, \tau)$, the rib/membrane thickness, and in any case[18] has to be $\Delta r_1 < \Delta r_{1\max} = f\lambda/\rho$, where $\rho$ is the detector size.

The two conditions above in turn determine the diffraction-limited detector size ($\rho_{\mathrm{d}} = f\lambda/\Delta r_1 \geq \rho$) and the diffraction-limited detector sampling ($\Delta r = f\lambda/W_{\mathrm{d}}$), to be possibly resampled at the actual detector resolution.

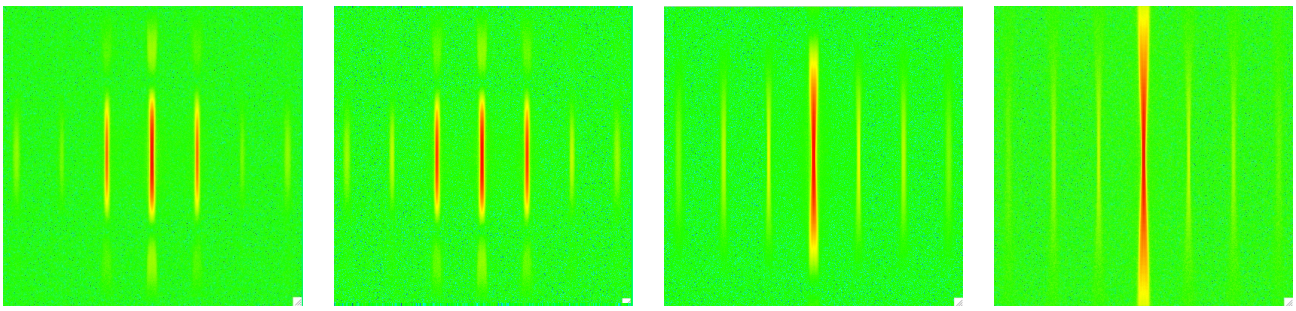

a) b) c) d)

Figure 16. Simulated diffraction patterns of a SPO MM with the same characteristics of Fig. 14, at $\lambda = 220$ nm, in-focus. Fig. 14a) on-axis. This figure, a) $\phi_x = 7$ arcmin, b) $\phi_x = 11$ arcmin, c) $\phi_y = 7$ arcmin, and d) $\phi_y = 11$ arcmin. We note the increasing relevance of the secondary peaks for increasing $\phi_x$, and the broadening in the vertical direction for increasing $\phi_y$.

Finally, we can simulate the effects of an *off-axis* source by a small angle $\phi_x$ and/or $\phi_y$: because in double reflection the angular deviation remains $4\alpha$ regardless of the off-axis angle, the optical paths throughout the module remain unchanged and it would in principle be sufficient to add to the exponent in Eq. 25 a wavefront tilt term, $\phi_x x_1 + \phi_y y_1$. However, when the module is seen off-axis by $\phi_x$, the rib vignetting becomes more severe and reduces the pore width. Also when the module is tilted by $\phi_y$, the pore height is reduced by the same amount: both aperture reductions follow the vignetting factors in Eq. 16. At the same time, the rib and membrane thickness appear to be increased by the same amount. In the case $L_1 = L_2$, we can therefore write

$$w' = w - 2L\phi_x, \tag{27}$$
$$t' = t + 2L\phi_x, \tag{28}$$
$$h' = h - 2L\phi_y, \tag{29}$$
$$\tau' = \tau + 2L\phi_y, \tag{30}$$

so the pore pitch values $(w+t,\, h+\tau)$ do not vary. One can account for the off-axis obstruction simply replacing $w, h, t$, and $\tau$ with the primed quantities, in the definition of $\chi_{\rm P}(\underline{r}_1)$: in the $\phi_x$ rotation, the misalignment affects the relative intensity of secondary peaks, but leaves the peak positions unchanged (Fig. 16, a, b). Increasing $\phi_x$, in contrast, the peaks are broadened in the vertical direction (Fig. 16, c, d) because the interference is essentially incoherent in the radial direction for an imperfectly monochromatic source.

Similarly we can redefine the clear aperture for a mirror design with a filling factor[13] different from 1, or $w, t$ variable along the polar angle.[4] However, this will be treated in a next phase of this project.

## 5. X-RAY SCATTERING AND SURFACE TOPOGRAPHY ANALYSIS

### 5.1 Interpretation of X-ray scattering (XRS) data

Analysis of X-ray data of SPO single pores and stacked mirror modules is of great value in understanding the properties of X-ray reflection and scatter. Collecting, combining and analyzing the available measurements performed on the ATHENA mirrors allow for an overall picture of the SPO mirror module performance and will be directly applicable to on-ground and in-flight calibration.

Several data taken at the PTB lab at the BESSY synchrotron light source[11] on SPO samples are *detector scans* at fixed incidence angle $\theta_{\rm i}$ and fixed X-ray energy, varying the off-surface scattering angle $\theta_{\rm s}$. This kind of scattering scan returns quantitative information not only on the layered structure, but also on the roughness power spectral density[10] (PSD). In fact, one of the classical results of the first order scattering theory is that the distribution of the scattered (i.e., non-specular, at $\theta_{\rm s} \neq \theta_{\rm i}$) intensity is directly proportional to the surface PSD at the spatial wavelength

$$l = \frac{\lambda}{\cos\theta_{\rm i} - \cos\theta_{\rm s}}, \tag{31}$$

if the smooth-surface approximation $4\pi\sigma \sin\theta_\mathrm{i} \ll \lambda$ is fulfilled. Sometimes we use the spatial frequency $\nu = 1/l$ instead of $l$. Measuring the X-ray intensity at variable $\theta_\mathrm{s}$ values, one can immediately retrieve a measurement of the surface finishing PSD, to be compared to the one that can be computed from a direct metrological approach, such as with atomic force microscopy (AFM) or phase shift interferometry (PSI) techniques. Unlike direct metrology, however, the measurement in X-rays is much more representative because the fraction of illuminated surface is much larger than the few mm$^2$ typically sampled with topographical instrumentation for roughness.

When reflective coatings are used, X-rays penetrate the thin layers they consist of and get scattered by the roughness of each interface. In addition to the expected constructive interference in the specular direction, the scattered radiation in non-specular directions interferes giving rise to fringes in the scattering plot, and this makes the scattering diameter more complicated to interpret.[21] An example of XRS scan of a SPO MM taken at BESSY is shown in Fig. 17, at 6 keV and $\theta_\mathrm{i} = 0.6$ deg. The last stacked plate was used in order to avoid vignetting effects from the pore structure: the surface was coated with a Ir/$B_4C$ graded multilayer coating deposited at DTU, with 5 layer pairs of thickness increasing from the substrate to the surface, plus two additional capping layers.[22] The XRS diagram is characterized by a broad core resulting from the convolution of the module PSF with the spatial resolution of the detector ($\Delta\theta_\mathrm{s} \approx 250$ arcsec). Hence, no information on the low-angle PSF can be extracted from this dataset. In contrast, the right wing of the XRS scan contains the required information on the surface roughness. Moreover, small oscillations in the XRS diagram are clearly seen.

In a multilayer-coated surface, a number of interfaces is present and each PSD contributes to build up the XRS diagram. In addition, the roughness profiles of different interfaces can be partially correlated, i.e., the roughness can be replicated from layer to layer not only in amplitude, but also in phase. Depending on the spatial wavelength and the deposition process details, the growth of the next deposited layer can either amplify or relax roughness features.[23] Amplification typically occurs at mid- ($10\ \mu\mathrm{m} > l > 1\ \mu\mathrm{m}$) spatial wavelengths, triggering a roughness growth throughout the multilayer with a high replication ratio and correlated interfaces. Relaxation usually dominates at small ($l < 1\ \mu\mathrm{m}$) spatial wavelengths and yields interfaces with almost no growth – or even smoothing of the substrate's rough features – and a little or no correlation between interfaces. As a result, we may expect to have an XRS plot characterized by prominent fringes in the correlated roughness region (mid scattering angles) and a smoothly decreasing XRS diagram in the non-correlated roughness range (high scattering angles). Application of Eq. 31 shows us that the spectral range that can be explored with the scatter plot typically covers the spectral band 10 - 0.1 $\mu$m. In reality, Eq. 31 also shows that this wavelength range does not relevantly impact the HEW in the sensitivity band of ATHENA, which is chiefly determined by lower frequencies. These are, indeed, difficult to analyze in BESSY data for three reasons:

- the PSD typically increases rapidly for low spatial frequencies and the scattering merges with the specular peak;
- at very low frequencies, the smooth-surface approximation is no longer fulfilled and the first-order theory is no longer applicable;
- the detector resolution does not allow us to resolve the details of the PSF core.

The XRS detector scan provides, however, an independent confirmation of the PSD obtained from the metrology and returns quantitative information on the PSD evolution inside the coating. This allows us, in turn, to predict the HEW evolution at high energies. A direct measurement of the PSF would require a much higher resolution (e.g., achievable using a high-res X-ray diffracting crystal).

The interference of the scattered waves at the interfaces $j = 0, 1, \ldots, N$ (numbered from the substrate upwards) returns a quite complicated formula[21,23,24] to model the scattered intensity per radian, $\mathrm{d}I_\mathrm{s}/\mathrm{d}\theta_\mathrm{s}$:

$$\frac{1}{I_0}\frac{\mathrm{d}I_\mathrm{s}}{\mathrm{d}\theta_\mathrm{s}} = \frac{16\pi^2}{\lambda^3}\sin\theta_\mathrm{i}\sin^2\theta_\mathrm{s}\sqrt{R(\theta_\mathrm{s})R(\theta_\mathrm{i})}\left[\sum_{j=0}^{N} T_j P_j(\nu) + 2\sum_{j<m}(-1)^{(j+m)} C_{jm}(\nu) T_j T_m \cos(\gamma\Delta_{jm})\right], \tag{32}$$

where $R(\theta)$ is the single interface reflectivity (if the multilayer consists of two alternated materials), $I_0$ the direct beam intensity, $T_j$ the amplitudes of the electric field at the $j^{th}$ interface of the multilayer, $\Delta_{jm}$ the distance between the $j^{th}$ and the $m^{th}$ interface, $\gamma$ is the normal component of the scattering vector (including absorption

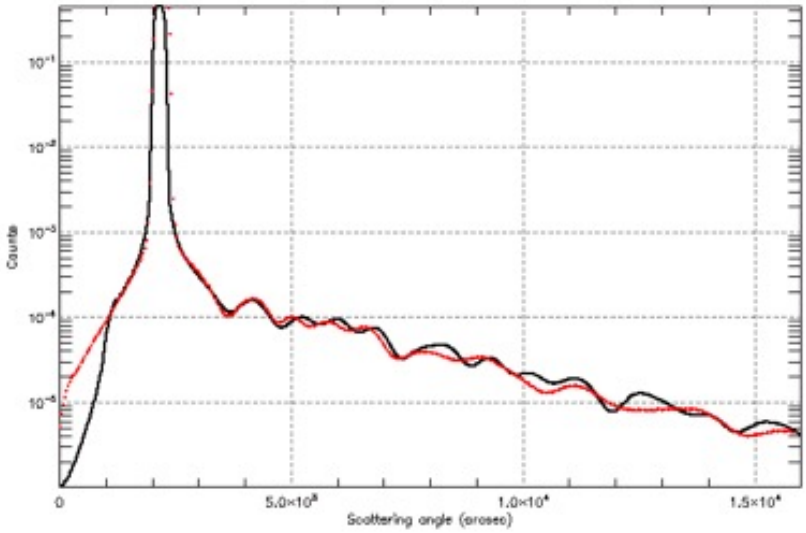


Figure 17. (red) Measured detector scan at 6 keV and 0.6 deg of a SPO plate coated with a graded $Ir/B_4C$ multilayer. (black) the XRS modeled diagram computed using Eq. 32.

via the imaginary part of the refractive index). Finally, $P_j$ is the PSD of the $j^{th}$ multilayer interface and $C_{jm}$ is the real part of the cross-correlation function between the $j^{th}$ and the $m^{th}$ interface (see[24] for further details).

The distribution of the electric fields $T_j$ can be computed from the transmittance and the reflectivity at each interface of the multilayer (s-polarized in the setup adopted at BESSY). In our case, most of the reflection at 6 keV and 0.6 deg occurs at the outermost $Ir/B_4C$ interface, and this explains why the interference fringes are not very pronounced. The computation of the $P_j$ and of the $C_{jm}$ functions is much more complicated as one needs to model the roughness evolution in the multilayer in terms of 6 growth parameters.[23,24] To this end, we would need to compare the roughness of a SPO plate before ($P_0$) and after ($P_N$) coating, with two possible results: that i) the PSD is unchanged after coating deposition or ii) the PSD has changed after coating. In the first case, we can distinguish between two sub-cases:

1. $P_j = C_{jm} = P_N$, for all $j, m$: completely coherent replication of the roughness topography of the substrate throughout the multilayer, XRS diagram characterized by pronounced peaks.

2. $P_j = P_N$, $C_{jm} = 0$, for all $j, m$: no evolution of the PSD in the multilayer, no profile correlation between couples of interfaces, XRS diagram smoothly decreasing without peaks.

| **Parameter** | **1$^{st}$ King model** | **2$^{nd}$ King model** |
|---|---|---|
| $A$ (nm$^3$) | $2 \times 10^5$ | 18 |
| $\mathcal{L}_c$ ($\mu$m) | 1000 | 0.3 |
| $n$ | 1.8 | 2.2 |

Table 1. PSD parameters used to fit the XRS scan in Fig. 17. In the first King profile, other combinations of the $A$ and the $\mathcal{L}_c$ parameter values are also possible, because the substrate is in the power-law regime for all the spatial frequencies considered. The parameters of the second King profile are, in contrast, well constrained by the XRS scan.

At this stage, the PSD could be measured only after coating, measurements of SPO plates before coating are planned but not available yet; hence, the evolution in the multilayer could not be modeled. In this case, however, using Eq. 32 we find that a single PSD in the shape of a double King profile,

$$P_N(\nu) = \frac{A}{[1 + (\nu \mathcal{L}_c)^2]^{n/2}}, \tag{33}$$

returns a modeled XRS diagram that matches very well the experiment (Fig. 17), indicating a negligible roughness growth *at least* in the layers where the electric field has an appreciable amplitude. In Eq. 33, $A$ is a normalization constant, $\mathcal{L}_c$ is the knee wavelength and $n$ is a spectral index of the power-law regime ($\nu \gg 1/\mathcal{L}_c$). Two King functions are superimposed: one to account for the typical power-law trend of the substrate, which is probably constant in the multilayer in the low frequency range, and another to represent the roughness excess in the micron range, probably evolving throughout the multilayer. The parameters that return the best match with the experimental data are listed in Tab. 1. The fringe height is matched by the assumption $P_j = P_N$ and $C_{jm} = 0.75 P_N$ for all $j, m$. The best-fit PSD is shown in Fig. 18 (black dashed line).

Even if the modeling-measurement accord (Fig. 17) is satisfactory, there is some residual mismatch of peak position, probably caused by some fluctuation of the layer thickness. This is not exactly known and that should be derived separately from the accurate fit of the reflectivity scan, but this does not affect the PSD that is inferred. The $n$ value from the first King model, mostly inherited by the substrate, is the typical one of silicon wafers, and the PSD – in the 1000 - 10 $\mu$m crucial range – is better than the one of commercial wafers[25] by a two-fold factor.

### 5.2 Surface metrology and HEW trend modeling

To double-check the parameter values obtained in the previous section, roughness topography measurements have been taken on a single silicon plate coated with the same multilayer recipe. Unlike the SPO stack tested at BESSY, this sample did not withstand any lithographic process.[26] However, most of the reflection at 6 keV and 0.6 deg occurs at the first Ir/$B_4C$ interface and so the XRS diagram should not be affected by any possible damage at the outer $B_4C$/vacuum interface.

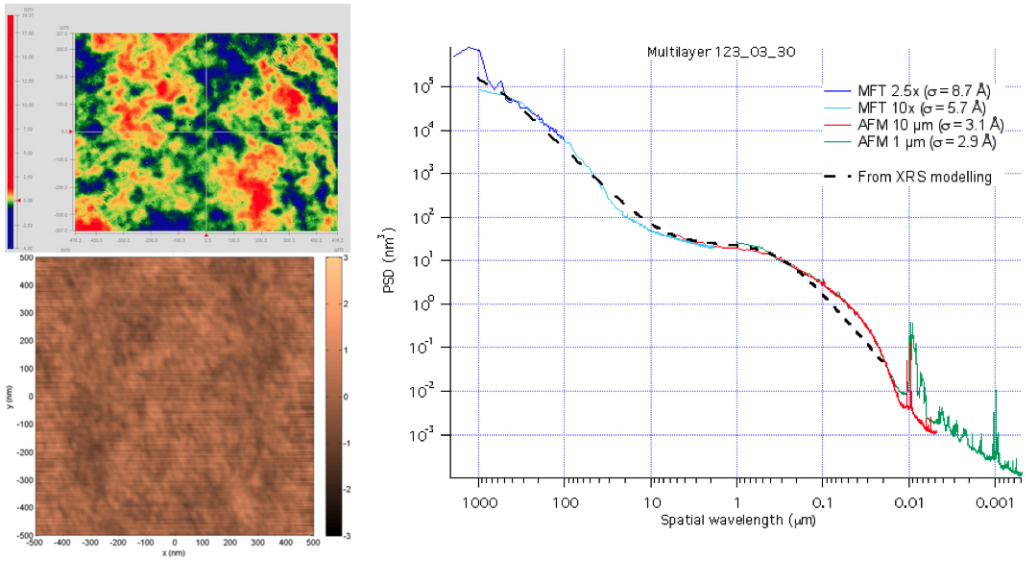


Figure 18. Measured power spectral density on the reflective side of the ribbed plate with a multilayer from MFT measurements (top, left) and AFM measurements (bottom, left). The PSDs measured with the different instruments at different magnifications are in excellent mutual agreement (right). The dashed line represents the PSD inferred from the XRS modeling described in Sect. 5.1.

The surface topography measurements have been performed using the MFT phase shift interferometer[27] at INAF/OAB, covering the low-frequency roughness range with the 2.5× and 10× magnification objectives. The high-frequency roughness has been characterized using the AFM operated at DTU.[28] The PSDs computed in the respective spatial frequency windows of sensitivity show a very good mutual agreement (Fig. 18). We clearly notice that the usual power-law trend, typical of polished substrates, is modified at spatial wavelengths 10 - 0.01 $\mu$m. The roughness excess is probably caused by the silicon oxide or the reflective coating, but this will be understood from subsequent measurements of roughness on samples before coating. We anyway find that

the PSD modeled from the XRS scan (Fig. 17) is in good agreement with the metrological measurement, which suggests the lift-off process on the module tested at BESSY not to have degraded the *interfacial* roughness (no information can be extracted at 6 keV about the outer surface roughness, however).

We now have a first measurement of the SPO MM surface finishing over a quite broad range of spatial wavelengths. Assuming this process to be representative of the surface smoothness of all the silicon plates, we can preliminarily infer the expected degradation of the HEW at 1 keV (where the specified value is $< 5$ arcmin) and at 6 keV (HEW <10 arcsec). This can be done in several ways. One is performing the complete computation of the PSF accounting for the roughness in a self-consistent way,[18] but this requires the exact measurement of the mirror shape errors in the longitudinal direction. For our scopes, a fast assessment of the scattering term of the HEW, $H(\lambda)$, is sufficient to determine if the mirror surface is smooth enough.

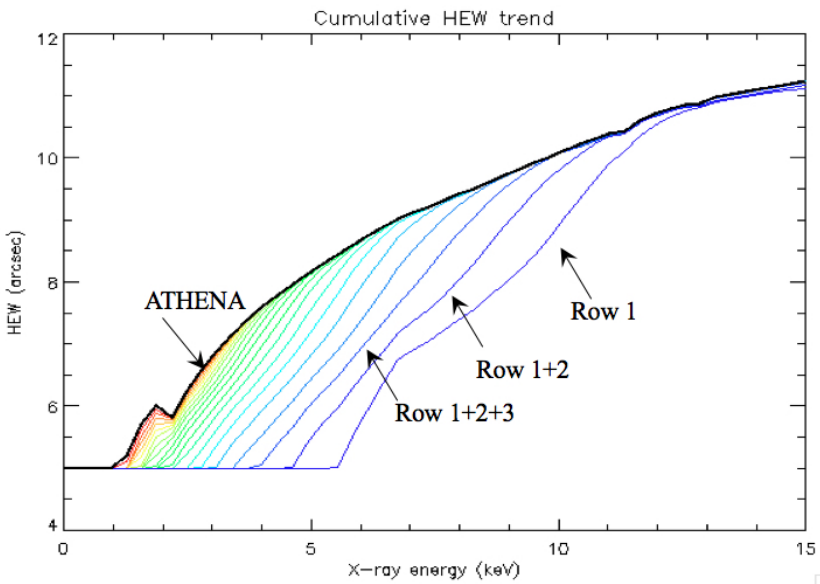


Figure 19. The average computed HEW as a function of the X-ray energy for the entire ATHENA telescope (black line), assuming a simple coating of Ir (11 nm) and $B_4C$ (8 nm). The colored lines are the cumulated contributions of the row 1, row 1+2, row 1+2+3... increasing from blue to red.

The HEW is usually an increasing function of the energy and of the incidence angle. Fortunately, the mirror plate reflectivity suddenly drops down beyond a critical incidence angle, and this sets the maximum possible degradation of the HEW at an assigned X-ray energy. In fact, the scattering term of the HEW increases as a function of the $\sin\theta_{\rm i}/\lambda$ ratio, but the upper bound for $\theta_{\rm i}$ is obviously the iridium critical angle, which is proportional to $\lambda$. Therefore, the maximum possible HEW degradation caused by the scattering does not depend either on $\theta_{\rm i}$ or $\lambda$, but only on the surface PSD and the optical constants of the reflective layer. For example, taking the expression of the double-reflection HEW scattering term[29] for a power-law PSD, $P(\nu) = K_n/\nu^n$, measuring $K_n$ in $\mathrm{nm}^3\mu\mathrm{m}^{-n}$, and replacing the optical constants of iridium, we provide an upper limit for $H(\lambda)$:

$$H(\lambda) < 5900 \left[\frac{K_n}{370(n-1)}\right]^{\frac{1}{n-1}} \text{arcsec}, \tag{34}$$

*regardless of the X-ray energy and the incidence angle.* In other words, the same roughness tolerances can be set for all the mirror modules, at all the mirror radii. Now, the low-frequency branch of the PSD (Fig. 18) well matches the values $n = 1.8$ and $K_n = 1\ \mathrm{nm}^3\mu\mathrm{m}^{-1.8}$, yielding $H(\lambda) < 5$ arcsec. This is in line with the requirement that HEW(1 keV) $< 5$ arcsec and HEW(6 keV) $< 10$ arcsec, assuming the figure and the scattering HEWs to add up linearly[18] (a dedicated argument on this point can be found in a previous paper[30]). The measured PSD therefore seems to be consistent with the scattering tolerances for ATHENA.

As a further step, we now deal with a more accurate evaluation of the predicted HEW trend for ATHENA, following the same method used a few years ago for IXO:[25] we computed the $H(\lambda)$ function from the measured

PSD, added a 5 arcsec of figure error HEW, and finally averaged the HEW trends over the computed effective areas of the 20 mirror module rows of the reference design,[12] in the 0.1-15 keV X-ray energy band. To compute $H(\lambda)$ down to 1 keV, the PSD had to be extrapolated down to a spatial wavelength of 1 cm, prolonging the measured power-law trend (the continuation of the power-law regime to the cm spectral range is usually observed on superpolished surfaces). For simplicity, the HEW values have been computed over the 40 arcmin field of view of ATHENA, but increasing the field does not affect the computation significantly: for example, doubling the field increases the values by less than 0.25 arcsec. The results are shown in Fig. 19: the largest radii (corresponding to the red lines) only contribute to the HEW at very low energy, while at high energy the inner radii (blue lines) dominate, but the scattering is moderated by the shallow incidence angles. At 6 keV, the predicted HEW is 8.5 arcsec, i.e., within the prescribed limits. The presence of the PSD "hump" at 1 - 0.01 $\mu$m (Fig. 18) actually causes an increase of the HEW beyond the prediction of Eq. 34, but it only affects the HEW at energies beyond 10 keV. The effect of this roughness excess on the effective area of ATHENA has still to be assessed, but this will be done in a next phase of this project.

## 6. VERY FIRST MAGNETIC DIVERTER SIMULATIONS

The soft ($<$ 1 MeV) proton flux on the detectors represents a major source of background in the cosmic environment outside the radiation belts.[31] The problem of evaluating the impact of the soft proton background was studied modeling the XMM spacecraft with the GEANT4 simulation package,[32] but the observed flux to the focal plane appeared to exceed the simulation results. The problem was in that the physical process used in GEANT4 to explain the proton reflection off the mirror assembly was assumed to be the multiple proton scattering in the Coulombian field of the atomic nuclei of the reflective layer. As a matter of fact, more efficient processes, such as the Firsov-Remizovich scattering[33] had already been proposed since the 60's to justify the reflection of soft protons off grazing incidence mirrors.

A deviation of charged particles without affecting the propagation of electromagnetic radiation can be effectively obtained by an intense magnetic field. A magnetic electron diverter was designed and realized[34] onboard Swift/XRT, by positioning permanent magnets at the exit pupil of the JET-X module in correspondence of the spider spokes. Although effective for electrons, the level of magnetic fields reached in the space crossed by the electrons would have been insufficient to deflect protons, which are almost 2000 times heavier.

The magnetic field required to obtain a deflection of an angle $\theta$ over a path of length $L$ of a particle with charge $e$, mass $m$, and kinetic energy $K$ is:[35]

$$B = \theta \frac{\sqrt{2mK}}{eL}, \tag{35}$$

and, assuming to have a proton beam – e.g., characterized by a divergence equal to the maximum incidence angle on the optics, 1.7 deg – to be diverted out of the field of view of the WFI, we take $\theta \approx 2$ deg, a magnet axial length $L = 15$ mm, and a maximum kinetic energy $K = 100$ keV, so we obtain a required magnetic field level of $B \approx 1000$ G. Higher kinetic energies clearly require higher values of $L$ or $B$. However, it was estimated[36] that protons with $K > 100$ keV, after the energy losses in the detectors' optical filters, would deliver an energy outside the ATHENA energy band and would thereby be discarded as proton events.

Even though Eq. 35 can provide a useful guess on the magnetic field level required, it was derived in the hypothesis of a uniform magnetic field, which is extremely difficult to obtain. The magnetic field from assembly of permanent magnets has the advantages of no power consumption and high stability in time, but is in general non-uniform. For this reason, the design and the performance verification of a proton diverter should be based on a MonteCarlo method. We have already developed such a code in past years to simulate the effect of an azimuthal magnetic field for the SIMBOL-X X-ray telescope.[37]

In order to extend the previous work and design a magnetic diverter for ATHENA, all the following requirements have to be fulfilled:

- The magnetic field has to operate an effective diversion/deviation of the particle beam (protons and electrons) out of the detector area, for $K < 100$ keV.

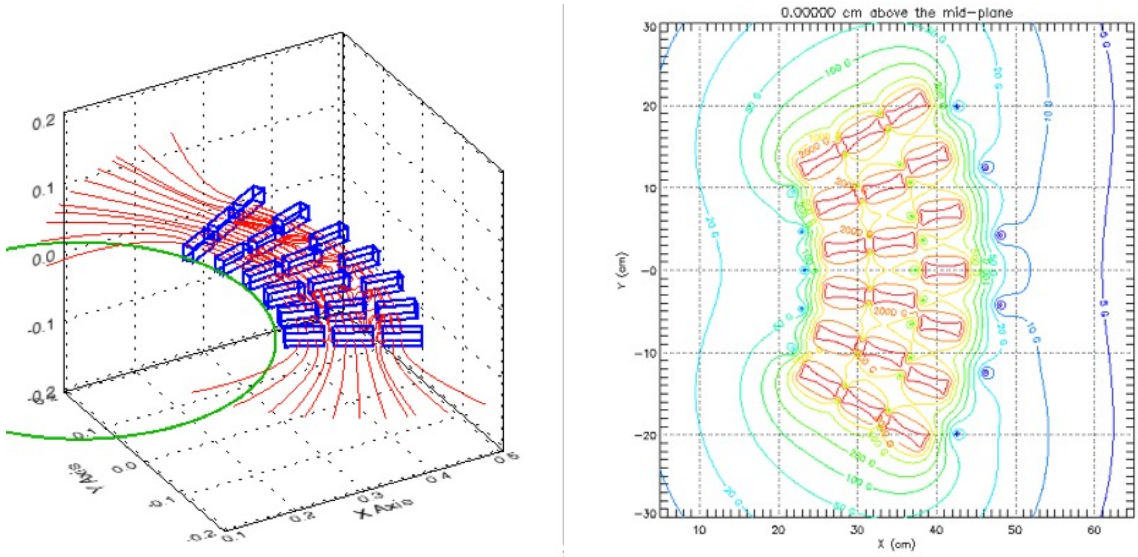


a) b)

Figure 20. a) Computed field lines for 3 lines of magnets on a single petal of ATHENA optics. The green circle represents the inner rim of the optics. b) Isocontours of the magnetic field intensity in the mid-plane of the diverter. The magnetic bar in the upper-left corner is subject to a torque of 0.03 Nm in CCW sense, a force of -6.7 N along $x$ direction, and of -16.8 N along $y$.

- The magnetic field should not refocus stray protons towards the detectors.
- The magnetic assembly should have zero total dipole moment to avoid torques that would affect the spacecraft orientation by interaction with the solar magnetic field in the L2 point.
- The magnetic field should decrease rapidly moving away from the diverter to avoid disturbance to detectors or the related circuity.
- The diverter should not conflict with the mechanical mounting of the optics.
- The diverter should not obstruct the X-ray flux.
- The diverter should fulfill the allocated mass limits.

The initial magnetic configuration under test is the one shown in Fig. 20a: we have simulated magnetic bars of 50 mm radial, 12 mm azimuthal, and 15 mm axial size in the spaces between MMs in the three innermost rows of a single petal as per ESA's current design.[12] The simulated magnetic material is a Nd-Fe-B sintered alloy with a magnetic remanence 1.2-1.3 T and a coercitive strength -950 kA/m. The total magnet mass for the ATHENA optics using magnetic bars of this type can be estimated around 60 kg, plus the structures needed to hold them in place.

The magnetic field computation (details are reported elswhere[38]) show that in the test configuration adopted here the magnetic field intensity in the space between magnets (i.e., in the regions where protons can be reflected) takes on values close to 0.1 T or higher, more or less between the yellow and the orange contours in Fig. 20b. Inside the magnetic material, the B-H variation is perfectly superposed to the nominal hysteresis cycle of the material. The magnetic field decreases rapidly along the $z$-axis, and at only a 10 cm distance from the MD mid-plane, it is below a few mT. On the focal plane, 12 m distant, the magnetic field is completely negligible.

Following Eq. 35, the simulated levels of magnetic field would be sufficient to fully deflect a collimated beam. However, in reality the proton beam is only *partly* collimated, and the proton reflection is not perfectly elastic: this introduces a relevant spread in the exit spectrum and directions that make the prediction of the proton trajectory less deterministic. In fact, a divergent beam would require a comparatively higher magnetic field intensity because the $\theta$ angle appearing in Eq. 35 is the angular size of the detector to be avoided *plus* the initial divergence angle of the proton. There is, as of today, some experimental work about the distribution of linear moments of protons after reflection in grazing incidence,[39] but a complete understanding of the proton scattering physics, or even a complete empirical description of the phenomenon, is still lacking.

An alternative approach, reported in a paper of this volume,[40] faces the problem using a particle simulator developed at INAF-IASF Bologna, based on GEANT4 libraries, able to tune different physical processes at work in the grazing reflection of charged particles. The results simulated for XMM-Newton, once compared to the measured background by the EPIC detectors, provide clues in favor of the Firsov-Remizovich model as a good candidate to describe the proton scattering off grazing-incidence optics. Hopefully, proton scattering experiments in the next future should provide a description of the scattering distribution as a function of the kinetic energy, the incidence angle, and the coating materials, to validate the scattering models. This should in turn provide an accurate and reliable input to the magnetic diverter simulator.

## 7. CONCLUSIONS

A set of simulation and modeling tools are being developed by a collaboration between INAF-OAB and DTU Space, covering crucial topics of the SPO-based design of the ATHENA optics, including geometrical optics methods and physical optics simulations, particle tracing, and scattering predictions in very good agreement with surface metrology and X-ray measurements taken at BESSY. The activities will be further developed in the next two years to support the design, the performance simulation, the realization, the integration, the alignment, and the verification of the ATHENA optical mirror assembly.

## ACKNOWLEDGMENTS

This work is supported by ESA/ESTEC (contract number 4000114410). We thank G. Valsecchi, G. Bianucci, and F. Marioni (Media-Lario Technologies) for useful discussions on the UV diffraction of SPO modules.

## REFERENCES

[1] Bavdaz, M., Wille, E., Shortt, B., Fransen, S., et al., "The ATHENA optics development," Proc. SPIE 9905, 990525 (2016)

[2] Collon, M.J., Vacanti, G., Günther, R., Yanson, A., et al., "Silicon pore optics for the ATHENA telescope," Proc. SPIE 9905, this conference (2016)

[3] Van Speybroeck, L.P., Chase, R. C., "Design parameters of paraboloid-hyperboloid telescopes for X-ray astronomy," Appl. Opt. 11(2), 440 (1972)

[4] Wille, E., Bavdaz, M., Oosterbroek, T., et al., "Silicon Pore Optics Mirror Modules for Inner and Outer Radii," Proc. SPIE 9603, 96030L (2015)

[5] Conconi, P., Campana, S., "Optimization of grazing incidence mirrors and its application to wide-field X-ray telescopes," A&A 372, 1088-1094 (2001)

[6] Knudsen, E.B., Nielsen, M.M., Haldrup, K., et al., "Novel applications of the x-ray tracing software package McXtrace," Proc. SPIE 9209, 92090B (2014)

[7] Della Monica Ferreira, D., Knudsen, E.B., Westergaard, N.J., Christensen, F.E., et al., "Simulating X-ray telescopes with McXtrace: a case study of ATHENA's optics," Proc. SPIE 9905, 990575 (2016)

[8] Westergaard, N.J., "MT_RAYOR: a versatile raytracing tool for x-ray telescopes," Proc. SPIE 8147, 81470Y (2011)

[9] Mieremet, A.L., Beijersbergen, M.W., "Fundamental spatial resolution of an x-ray pore optic," Appl. Opt. 44(33), 7098 (2005)

[10] Stover, J.C., "Optical scattering: measurement and analysis," SPIE Press (1995)

[11] Collon, M.J., Vacanti, G., Günther, R., Yanson, A., et al., "Silicon Pore Optics development for ATHENA," Proc. SPIE 9603, 96030K (2015)

[12] Oosterbroek, T., "ATHENA telescope reference design and effective area estimates," ESA document SRE-F/2014-033 (2014)

[13] Spiga, D., "Optics for X-ray telescopes: analytical treatment of the off-axis effective area of mirrors in optical modules," A&A 529, A18 (2011)

[14] Spiga, D., Cotroneo, V., Basso, S., Conconi, P., "Analytical computation of the off-axis effective area of grazing incidence X-ray mirrors," A&A 505(1), 373 (2009)

[15] Spiga, D., "Effective area analytical computation for segmented optics," INAF/OAB int. rep. 16/2014 (2014)

[16] Windt, D. L., "IMD - Software for modeling the optical properties of multilayer films," Computer in Physics 12, 360 (1998)
[17] Spiga, D., Raimondi, L., "X-ray optical systems: from metrology to Point Spread Function," Proc. SPIE 9209, 92090E (2014)
[18] Raimondi, L., Spiga, D., "Mirrors for X-ray telescopes: Fresnel diffraction-based computation of point spread functions from metrology," A&A 573, A22 (2015)
[19] Tayabaly, K., Spiga, D., Sironi, G., Canestrari, R., et al., "Computation and validation of two-dimensional PSF simulation based on physical optics," Proc. SPIE 9577, 957709 (2015)
[20] Spiga, D., Tayabaly, K., "Out-of-focus image of a paraboloidal mirror: analytical description in far-field and near-normal approximations," INAF/OAB int. rep. 09/2014 (2014)
[21] Spiga, D., "Development of multilayer-coated mirrors for future X-ray telescopes," Ph.D. dissertation (2005)
[22] Massahi, S., Della Monica Ferreira, D., Christensen, F.E., Shortt, B., et al., "Development and production of a multilayer-coated x-ray reflecting stack for the Athena mission," Proc. SPIE 9905, 99055P (2016)
[23] Canestrari, R., Spiga, D., Pareschi, G., "Analysis of microroughness evolution in X-ray astronomical multilayer mirrors by surface topography with the MPES program and by X-ray scattering," Proc. SPIE 6266, 626613 (2006)
[24] Salmaso, B., Spiga, D., Canestrari, R., Raimondi, L., "X-ray scattering of periodic and graded multilayers: comparison of experiments to simulations from surface microroughness characterization," NIM-A 710, 106 (2013)
[25] Spiga, D., Pareschi, G., "Surface smoothness requirements for the IXO X-ray telescope," Proc. SPIE 7437, 74371M (2009)
[26] Massahi, S., Girou, D., Della Monica Ferreira, D., et al., "Investigation of photolithography process on SPOs for the ATHENA mission," Proc. SPIE 9603, 96030M (2015)
[27] Tayabaly, K., Stover, J.C., Parks, R.E., et al., "Use of the surface PSD and incident angle adjustments to investigate near specular scatter from smooth surfaces," Proc. SPIE 8838, 883805 (2013)
[28] Della Monica Ferreira, D., Jakobsen, A.C., Massahi, S., Christensen, F.E., et al., "X-ray mirror development and testing for the ATHENA mission," Proc. SPIE 9905, 99055K (2016)
[29] Spiga, D., "Analytical evaluation of the X-ray scattering contribution to imaging degradation in grazing-incidence X-ray telescopes," A&A 468, 775 (2007)
[30] Tayabaly, K. , Spiga, D. , Canestrari, R. , Bonnoli, G., et al., "Roughness tolerances for Cherenkov telescope mirrors," Proc. SPIE 9603, 960307 (2015)
[31] Dichter, B.K., Woolf, S., "Grazing angle proton scattering: effects on Chandra and XMM-Newton X-ray telescopes," IEEE Trans. Nucl. Sci. 50(6) 2292 (2003)
[32] Nartallo, R., Daly, E., Evans, H., et al., "Low-angle Scattering of Protons on the XMM-Newton Optics and Effects on the On-Board CCD Detectors," IEEE Trans. Nucl. Sci. 48(6) 1815 (2001)
[33] Firsov, O.B., "Reflection of fast ions from a dense medium at glancing angles," Sov. Phys. Doclady 11(1), 732 (1967)
[34] Willingale, R., "An electron diverter for the Swift Telescope," XRA study note XRT-LUX-RE-011/1, University of Leicester (2000)
[35] Turner, M., "A magnetic diverter for Charged Particles on XEUS," ESA rep. SCI-SA/AP/06/0412cv (2006)
[36] Molendi, S., Gastaldello, F., Rossetti, M., Spiga, D., Tiengo, A., "A quick and not entirely clean estimate of the Soft Proton impact on Athena," INAF-IASF technical note (2015)
[37] Spiga, D., Fioretti, V., Bulgarelli, A., Dell'Orto, E., et al., "A magnetic diverter for charged particle background rejection in the SIMBOL-X telescope," Proc. SPIE 7011, 70112Y (2008)
[38] Spiga, D., Mattaini, E. , Parodi, G., Ottolina, M., Fioretti, V., Tiengo, A., "Notes on the development of a magnetic diverter for the SIMBOL-X X-ray telescope," INAF/OAB int. rep. 06/2009 (2009)
[39] Diebold, S., Tenzer, C., Perinati, E., et al., "Soft Proton Scattering Efficiency Measurements on X-Ray Mirror Shells," Exp. Astr. 39(2), 343 (2015)
[40] Fioretti, V., Bulgarelli, A., Malaguti, G., Spiga, D., Tiengo, A., "Monte Carlo simulations of soft proton flares: testing the physics with XMM-Newton," Proc. SPIE 9905, 99056U (2016)